

# Equilibrium Initialization and Stability of Three-Dimensional Gas Disks

Hsiang-Hsu Wang<sup>1,2\*</sup>, Ralf S. Klessen<sup>2,5</sup>, Cornelis P. Dullemond<sup>1</sup>, Frank C. van den Bosch<sup>4</sup>, Burkhard Fuchs<sup>3</sup>

<sup>1</sup>*Max-Planck-Institut für Astronomie, Königstuhl 17, D-69117 Heidelberg, Germany*

<sup>2</sup>*Zentrum für Astronomie der Universität Heidelberg, Institut für Theoretische Astrophysik, Albert-Ueberle-Strasse 2, 69120 Heidelberg, Germany*

<sup>3</sup>*Zentrum für Astronomie der Universität Heidelberg, Astronomisches Rechen-Institut, Mönchhofstr. 12-14, 69120 Heidelberg, Germany*

<sup>4</sup>*Department of Physics and Astronomy, University of Utah, 115 South 1400 East, Salt Lake City, UT 84112, U.S.A.*

<sup>5</sup>*Kavli Institute for Particle Astrophysics and Cosmology, Stanford University, Menlo Park, CA 94025, U.S.A.*

Accepted by MNRAS 2010 April 28

## ABSTRACT

We present a new systematic way of setting up galactic gas disks based on the assumption of detailed hydrodynamic equilibrium. To do this, we need to specify the density distribution and the velocity field which supports the disk. We first show that the required circular velocity has no dependence on the height above or below the midplane so long as the gas pressure is a function of density only. The assumption of disks being very thin enables us to decouple the vertical structure from the radial direction. Based on that, the equation of hydrostatic equilibrium together with the reduced Poisson equation leads to two sets of second-order non-linear differential equation, which are easily integrated to set-up a stable disk. We call one approach ‘density method’ and the other one ‘potential method’. Gas disks in detailed balance are especially suitable for investigating the onset of the gravitational instability. We revisit the question of global, axisymmetric instability using fully three-dimensional disk simulations. The impact of disk thickness on the disk instability and the formation of spontaneously induced spirals is studied systematically with or without the presence of the stellar potential. In our models, the numerical results show that the threshold value for disk instability is shifted from unity to 0.69 for self-gravitating thick disks and to 0.75 for combined stellar and gas thick disks. The simulations also show that self-induced spirals occur in the correct regions and with the right numbers as predicted by the analytic theory.

**Key words:** galaxy: disc – galaxies: evolution – galaxies: structure – methods: numerical

## 1 INTRODUCTION

The stability of gas disks plays an important role in governing the structure of disk galaxies and in regulating their star formation rate. Although important insights can be obtained using perturbation theory (Toomre 1964, Lin & Shu 1964, Rafikov 2001), the onset of stability and its impact on the star formation and evolution of gas disks is best studied using hydrodynamical simulations. These can follow the non-linear behavior of the system, which cannot be addressed by linear analysis. With the recent advances in computing

power and the development of new numerical techniques, we are now in a good position to treat a three-dimensional, isolated galaxy self-consistently.

However, in order for a stability analysis to be meaningful and reliable, it is of paramount importance that one can specify equilibrium initial conditions. After all, if the initial disk is not in equilibrium, its relaxation during the first time-steps of the simulation may trigger instabilities that are of little relevance for our understanding of the stability of disk galaxies. Unfortunately, no analytical solution is known for the density, velocity field and temperature of a three-dimensional gas disk in hydrostatic equilibrium in the external potential of a dark matter halo and/or a stellar disk. Consequently, previous hydrodynamical simulations have ei-

\* E-mail: hhwang@mpia.de

ther started from non-equilibrium initial conditions, or have resorted to iterative techniques to set-up the initial conditions, at the cost of having little control over the resulting equilibrium configuration. In this paper we present a new method that allows one to compute the density and velocity structure of a realistic, isothermal, three-dimensional gas disk in hydrostatic equilibrium in an arbitrary external potential.

Hydrostatic equilibrium implies a balance between gravity and pressure. Gravity includes the self-gravity of the disk plus that of external components (i.e. dark matter halo, bulge, stellar disk, etc), while the pressure is given by an equation of state  $p = p(\rho_g, T)$ , with  $p$  being the gas pressure,  $\rho_g$  the gas density and  $T$  the temperature. The challenge is to find a  $\rho_g$ ,  $T$  and the velocity field,  $\vec{v}$ , such that the system is self-consistent (i.e., obeys the Poisson equation) and in hydrostatic equilibrium.

In the case of an isothermal, axisymmetric, perfectly self-gravitating disk (i.e., no external potential), the equilibrium disk has a  $\text{sech}^2$  distribution (Spitzer 1942) in the vertical direction, with a scale-height that is proportional to  $\sqrt{c_s^2/\rho_g(R, z=0)}$ , where  $c_s$  is the sound speed. Here, cylindrical coordinates,  $(R, \phi, z)$ , are used to describe the density field. This immediately shows that since  $\rho_g(R, z=0)$  is typically a decreasing function of radius, one generally expects the scale-height to be a function of  $R$ . In particular, in the case of a globally isothermal disk, the sound speed  $c_s^2 \propto T$  is constant in space, giving rise to a flaring disk, i.e., the scale-height increases with increasing  $R$  (Narayan & Jog 2002, hereafter NJ02; Agertz et al. 2009). Alternatively, if we want to initialize a disk with a constant scale-height, a radial temperature gradient needs to be introduced. Tasker & Bryan (2006) initialize their disks to be isothermal and to have a constant scale-height. As indicated above, this cannot be an equilibrium configuration. Consequently, the disk is expected to experience an unavoidable relaxation process which makes the initialization not well-controlled and might potentially contaminate the physics, e.g., star formation, gas dynamics etc., of interest. Agertz et al. (2009) set-up their isothermal disks based on the local total surface density of gas plus dark matter. Although the scale-height of their initial disk changes with radius, the local total surface density is not defined in a mathematical way and therefore elusive. In addition, their surface density does not follow an exponential profile.

An important assumption underlying Spitzer’s analysis is that the radial variation in the potential is negligible compared to that in the vertical direction. This assumption is supported by observation that disks typically have vertical scale-heights that are an order of magnitude smaller than their radial scale-length (van der Kruit & Searle 1981a,b). A well studied example is the Milky Way, whose scale-height is less than 200 pc for the cold gas (Jackson & Kellman 1974; Lockman 1984; Sanders et al. 1984; Wouterloot et al. 1990; see also Narayan & Jog 2002) and roughly 300 pc for the stars in the Solar neighborhood (Binney & Tremaine 2008, Kent, Dame & Fazio 1991), compared to a radial scale-length of  $\sim 3.5$  kpc. Throughout this paper we therefore follow Spitzer and consider disks to be ‘thin’, allowing us to treat their radial and vertical structure separately. Hence, we caution that our method is not valid for thick disk structures.

However, since we are mainly concerned with cold gas disks in this paper, this restriction is of little importance.

Springel, Matteo & Hernquist (2005) introduce a flexible solution for initializing a gas disk self-consistently. Basically, they solve Eq. (2), Eq. (3) and Eq. (24) (see Section 2) iteratively. First, they deploy a number of particles (say,  $2048 \times 64 \times 64$ ) on a distorted grid structure in the radial, the azimuthal and the vertical directions. Unlike the live particles, these particles are simply used as markers for mass distribution. Second, they compute the joint total potential and the resulting force field numerically with a hierarchical multipole expansion based on a tree code. Third, given the potential just computed, integrating Eq. (2) for a given midplane volume density,  $\rho_g(R, z=0)$ , gives the vertical structure of density. Fourth, adjust the midplane volume density to fulfill Eq. (24). Repeat the procedure between the second step and the fourth until the result converges.

Although this description is quite general and flexible, for several reasons, this is not commonly used in the grid-based codes which are featured with adaptive-mesh refinement (AMR). The first and also the most fundamental one is that the grid structure is normally unknown before we actually initialize the disk. Except the uniform-grid initialization, the grid structure is automatically generated based on the criterion for refinement. Second, for a fully parallelized code, the initial data is distributed over different processors and memory storages. This means that the data exchange between processors is necessary in order to fully compute the joint total potential. The situation becomes even more technically challenging when initializing with AMR. Third, The vertical structure of the gas disk depends only on the vertical potential difference (see Eq. (7) and Eq. (9) below). A description of the equatorial potential is enough for specifying the velocity field (See Eq. (13), Eq. (29) and the results shown in Sec. 3). In general, given the density distribution computed by the methods introduced in Section 2.2 together with the conclusion in Section 2.1, we are allowed to acquire the exact velocity field by Eq. (A.17) in Casertano (1983). Fully solving the Poisson equation becomes not necessary. Fourth, initializing a disk over distributed memories allow us to deal with a larger data set which cannot be fully contained in a single memory storage.

We propose a simple but very effective way of initializing a three-dimensional gas disk. This method can be easily incorporated into any existing code based on either a Lagrangian or Eulerian approach. No data exchange between processors is needed. Vertical density profile is obtained self-consistently without solving the full Poisson equation. We implement these ideas with the adaptive mesh refinement magnetohydrodynamics code RAMSES (Teyssier 2002) and apply our concepts to probe the onset of the disk instability. We modify the dispersion relation for the infinitesimally thin disk (Lin & Shu 1964) to be able to treat thick disks (Goldreich & Lynden-Bell 1965; Kim & Ostriker 2002a, 2006; Shetty & Ostriker 2006; Lisker & Fuchs 2009). The threshold value  $Q_{\text{th}}$  is then obtained semi-analytically. Previous studies on this subject are either focused on a small patch of a galaxy (2D/3D: Kim & Ostriker 2002a) or are globally two-dimensional but with the reduction of gravity included in the governing equations (Shetty & Ostriker 2006). In this paper, we revisit the subject as a test of our fully three-

dimensional isolated galaxy models. Models with or without stellar potential are investigated.

Galactic disks are comprised of stars and gas. Both components are coupled to each other via the Poisson equation. Since the stellar disk dominates the mass budget within the luminous disk, its presence has great impact on the scale-height of the gas disk as described in NJ02. A balanced initial condition depends not only on the correct vertical structure but also on the correct rotation velocity. To specify the rotation velocity needed, the mass enclosed within a certain radius must be under control. Although it is common practice to specify the functional form of the volume densities of 3D disks, we show that because of the flaring disk this typically results in a surface density profile that contains a central ‘hole’ (Agertz et al. 2009). This problem can be trivially avoided by specifying the desired surface density profile instead. We show that the corresponding volume density can easily be obtained using a simple iterative scheme. The surface density of the total gas (HI + H<sub>2</sub>) from observation (Leroy et al. 2008) typically follows an exponential profile in disk galaxies. This profile gives an analytic description of the total mass enclosed within a radius as well as a reasonable approximation for velocity field as shown by Eq. (29) below (Binney & Tremaine 2008).

Describing the stellar disk with a fixed background potential is at best an approximation to reality. The interaction between live stellar disk and gas can potentially destabilize the system (Rafikov 2001; Li, Mac Low & Klessen 2005a, 2005b, 2006; Kim & Ostriker 2007). After all, the gas is cold compared to the stellar disk and has highly non-linear response to the asymmetric stellar potential. The gravitational interplay between the collisionless stars and dissipative gas is important for a number of key questions in galactic dynamics. For example, what is the physical origin of grand design spirals? Or what initiates and regulates the formation of stars? Having access to well-controlled initial and environmental conditions is a prerequisite to discovering their causes.

This paper is organized as follows. The ideas of initializing a gas disk are outlined in Section 2. Details of the simulation parameters and test runs are described in Section 3. Axisymmetric instability of the disk is revisited in Section 4. The self-induced spirals due to swing amplification will be discussed in Section 5. A brief summary and the possible extension of this work is put in Section 6.

## 2 FORMULATION OF EQUATIONS

In this Section, we develop the required relations and equations to immerse a 3D gas disk in a preexisting static potential. Assuming that the gas disk and the preexisting potential share the same symmetry axis, cylindrical coordinates,  $(R, \phi, z)$ , are adopted to formulate the dynamics of the system. Axial-symmetry enables us to discard the terms describing the variation in azimuthal direction, i.e.,  $\partial/\partial\phi = 0$ . A gas disk which is in detailed balance should fulfill the following equations:

$$\frac{1}{\rho_g} \frac{\partial p}{\partial R} + \frac{\partial \Phi}{\partial R} = \frac{V_{\text{rot}}^2}{R}, \quad (1)$$

$$\frac{1}{\rho_g} \frac{\partial p}{\partial z} + \frac{\partial \Phi}{\partial z} = 0, \quad (2)$$

with  $\rho_g$ ,  $p$ ,  $V_{\text{rot}}$  and  $\Phi$  being the volume density of the gas, the gas pressure, the azimuthal rotation velocity (“rotation velocity” in short) and the joint total potential. Equation (1) describes that the gravitational pull in radial direction is counterbalanced by the centrifugal force and the pressure gradient. Equation (2) states that hydrostatic equilibrium along the symmetry axis, the  $z$ -direction, is achieved by the balance between vertical pull of the gravity and the pressure gradient in  $z$ .

To make the system self-consistent, the Poisson equation must be involved:

$$\nabla^2 \Phi = 4\pi G(\rho_g + \rho_{\text{DM}} + \rho_s), \quad (3)$$

with  $G$ ,  $\rho_{\text{DM}}$  and  $\rho_s$  being the gravitational constant, and the volume density of dark matter and stars. The total potential is comprised of the contributions from the dark matter halo, the stellar disk and the self-gravity of the gas, i.e.,  $\Phi = \Phi_{\text{DM}} + \Phi_s + \Phi_g$ . In addition, the ideal gas law provides the link between the gas density, the gas temperature and the gas pressure:

$$p = \rho_g(\gamma - 1)e(T), \quad (4)$$

where  $\gamma$  represents the ratio of the heat capacities (adiabatic index),  $e$  the specific internal energy and  $T$  the gas temperature. In the case of an ideal gas, the specific internal energy depends only on temperature, and is given by

$$e = \frac{1}{\gamma - 1} \frac{k_B T}{\mu m_p}, \quad (5)$$

with  $k_B$  being the Boltzmann’s constant,  $\mu$  the atomic weight and  $m_p$  the mass of a proton. However, to close the set of equations, we should either invoke the energy equation or an equation of state (EoS), which will be used to evolve the system.

A disk which is in hydrodynamic equilibrium should stay in its original state if we evolve the disk with the same equation of state which is used to set-up the disk. The numerical results throughout this paper are based on the isothermal equation of state, i.e.,

$$p = c_s^2 \rho_g, \quad (6)$$

with  $c_s$  being the sound speed, a temporal and spatial constant. Equations (1) to (6) then form the basis of our discussion. In this paper, all the disks are in detailed equilibrium with the isothermal EoS. If those disks are adopted to evolve with a cooling function or a polytropic EoS, we can make sure any change in temperature or dynamics is purely caused by a cooling or a heating source.

For a polytropic gas,  $p = K\rho_g^\Gamma$ , with  $\Gamma$  and  $K$  being constant, integrating Eq. (2) gives:

$$\rho_g(R, z) = \rho_g(R, z = 0) \left[ 1 - \frac{\Gamma - 1}{c_s^2(R, z = 0)} \Phi_z(R, z) \right]^{\frac{1}{\Gamma - 1}}, \quad (7)$$

where  $\Phi_z(R, z) = \Phi(R, z) - \Phi(R, z = 0)$  defines the vertical potential difference. We have used the fact that  $c_s^2 \equiv \partial p / \partial \rho_g = K\Gamma\rho_g^{\Gamma - 1}$  when approaching Eq. (7). Note that given  $\Gamma \neq 1$ , the internal energy has the following relation:

$$e(T) = \frac{K\rho_g^{\Gamma - 1}}{\gamma - 1}. \quad (8)$$

Combining Eq. (5) and Eq. (8) gives the temperature field

as a function of position if the gas disk is initialized with a non-isothermal EoS. As a special case, when  $\Gamma \rightarrow 1$ , Eq. (7) then converges to a form for the isothermal gas:

$$\rho_{\text{g}}(R, z) = \rho_{\text{g}}(R, z = 0) \exp\left(-\frac{\Phi_z(R, z)}{c_s^2}\right). \quad (9)$$

As we can see from Eq. (7) and Eq. (9), the vertical structure of gas disk depends on the gas properties in the midplane and the vertical potential difference.

To fully characterize a gas disk which is in detailed balance, we need to specify the velocity, the density and the temperature at every location in the beginning of the simulation. In the following sub-sections we study the general properties of the velocity and density field, which allows us to devise a simple, but effective method to initialize a 3D gas disk in hydrostatic equilibrium.

## 2.1 Azimuthal Rotation Velocity

In this sub-section, we treat the azimuthal rotation velocity as generally as possible. To make the notation concise, we drop the subscript of gas density,  $\rho_{\text{g}}$ , and restore the subscript after this sub-section. Without further assumption, integrating Eq. (2) from 0 to  $z$  gives:

$$\int_0^z \frac{1}{\rho} \frac{\partial p}{\partial z} dz = -\Phi_z(R, z). \quad (10)$$

By integrating Eq. (10) in parts, we have:

$$\frac{p(R, z)}{\rho(R, z)} = \frac{p(R)}{\rho(R)} \Big|_{z=0} - \int_0^z \frac{p}{\rho^2} \frac{\partial \rho}{\partial z} dz - \Phi_z(R, z). \quad (11)$$

Inserting Eq.(11) into (1), we get (see Appendix A for further details):

$$\begin{aligned} \frac{V_{\text{rot}}^2(R, z)}{R} &= \frac{1}{\rho} \frac{\partial p}{\partial R} + \frac{\partial \Phi(R, z)}{\partial R} \\ &= \frac{1}{\rho} \frac{\partial p}{\partial R} \Big|_{z=0} + \frac{\partial \Phi(R)}{\partial R} \Big|_{z=0} \\ &\quad - \int_0^z \left\{ \left( \frac{\partial \rho}{\partial z} \right) \frac{\partial}{\partial R} \left( \frac{p}{\rho^2} \right) - \left( \frac{\partial \rho}{\partial R} \right) \frac{\partial}{\partial z} \left( \frac{p}{\rho^2} \right) \right\} dz. \end{aligned} \quad (12)$$

Equation (12) shows that the rotation velocity is independent of height above or below the midplane so long as the integral vanishes. It is evident that gas with a barotropic equation of state, i.e.,  $p(\rho_{\text{g}})$ , fulfills this requirement. In addition, for an initially constant temperature ( $T$  is everywhere the same in the beginning) disk, the initial pressure is a function of volume density only and therefore the integral becomes zero. In this case, equation (12) can be simplified further:

$$V_{\text{rot}}^2(R, z) = R \frac{\partial \Phi}{\partial R} \Big|_{z=0} + (\gamma - 1) e \frac{\partial \ln \rho}{\partial \ln R} \Big|_{z=0}. \quad (13)$$

Equation (13) states that the process of specifying the initial velocity in 3D comes down to knowing the rotation velocity in the equatorial midplane.

## 2.2 Density Distribution

From now on, to avoid confusion, we restore the subscript for the gas density. To proceed further, we consider the gas layer

to be a very thin structure embedded in a static potential contributed by the background spherical dark matter and the stellar disk. Because the gas disk is observationally thin we neglect the radial variation compared to the vertical one (i.e.,  $|(\partial/\partial R(R\partial\Phi_{\text{g}}/\partial R))/R| \ll |\partial^2\Phi_{\text{g}}/\partial z^2|$ ). In Appendix E we show that this is a valid assumption for realistic gas disks. For an axisymmetric thin disk, the Poisson equation then reduces to (Binney & Tremaine 2008):

$$\frac{d^2\Phi_{\text{g}}}{dz^2} = 4\pi G\rho_{\text{g}}. \quad (14)$$

with  $\Phi_{\text{g}}$  being the potentials contributed by the gas. In the following, we focus only on disks with initially constant temperature, i.e., the rotation velocity required for equilibrium has no dependence on the height above or below the midplane.

### 2.2.1 Density Method

Differentiation Eq. (2) with respect to  $z$  and inserting Eq. (14) leads to a second-order non-linear differential equation:

$$\frac{d^2 p}{dz^2} - \frac{1}{\rho_{\text{g}}} \frac{d\rho_{\text{g}}}{dz} \frac{dp}{dz} + \rho_{\text{g}}(4\pi G\rho_{\text{g}} + \frac{d^2\Phi_{\text{s}}}{dz^2} + \frac{d^2\Phi_{\text{DM}}}{dz^2}) = 0, \quad (15)$$

with  $\Phi_{\text{s}}$  and  $\Phi_{\text{DM}}$  being the potentials contributed by the stellar disk and the dark matter, respectively. So far, Eq. (15) is still general with respect to any kind of equation of state. However, a single equation with two unknowns  $p$  and  $\rho_{\text{g}}$  is not solvable. To continue with Eq. (15), in this sub-section, we assume that the gas is barotropic, i.e.,  $p(\rho_{\text{g}})$ . Given density distributions of stars, the dark matter and the boundary conditions in the midplane:

$$\rho_{\text{g}}(R, 0) = \rho_0(R) \text{ and } \frac{d\rho_{\text{g}}}{dz} = 0, \quad (16)$$

equation (15) can be solved by numerical integration, e.g., using the Runge-Kutta method. For a single-component, self-gravitating, locally isothermal disk ( $c_s(R)$  can be a function of radius), Eq. (15) has an exact solution:

$$\rho_{\text{g}}(R, z) = \rho_0(R) \text{sech}^2(z/h), \quad (17)$$

with  $\rho_0(R)$  being the gas volume density in the midplane,  $h = \sqrt{c_s^2/2\pi G\rho_0}$  the scale-height and  $c_s$  the local isothermal sound speed. According to Eq. (17) and since the midplane volume density,  $\rho_0(R)$ , generally decreases with radius, to keep the scale-height a constant, the sound speed and therefore the temperature must be a function of radius.

Equation (15) is the simplified version of the formula derived by NJ02 (see also Kim et al. 2002a), where they investigated the vertical structure in a gravitationally coupled, multi-component galactic disk. It is important to notice that all calculations can be done locally without the need of exchanging information between processors and therefore greatly reduces the complexity of coding.

In principle Eq. (15) allows one to compute the density of the gas such that the disk initially is in hydrostatic equilibrium. The actual implementation using Eq. (15) does not guarantee the positivity of the density. In particular, at large radii  $\rho_{\text{g}}(R, z)$  is typically close to zero, and small errors due to the numerical integration often yield negative densities. This problem is especially relevant when using the adaptive-mesh refinement techniques.

Initializing a gas disk with AMR usually starts with the coarsest grid. A natural selection of the integration step is the cell size. Then a problem immediately rises when solving Eq. (15) to specify the volume density. Supposing that the cell size is much larger than the scale-height of the gas disk, the errors introduced by the coarse integration may lead to negative densities on the outskirts of the computation domain. One might think the integration can be done by using either adaptive integration intervals or simply a fixed integration interval which is much smaller than the cell size. However, the improvements only guarantee the convergence of the solution not the positivity. Nevertheless, because of the generality of Eq. (15), density method is still valuable for semi-analytic research.

### 2.2.2 Potential Method

In this sub-section, we develop another route for specifying the density distribution. We stress that the following derivation is only applicable to initially isothermal disks. With this constraint, integrating Eq. (2) gives:

$$\rho_g(R, z) = \rho_0(R) \exp\left(-\frac{\Phi_z(R, z)}{(\gamma - 1)e}\right). \quad (18)$$

Combining Eq. (14) and Eq. (18), a second-order non-linear equation for the vertical potential difference of gas is obtained:

$$\frac{d^2\Phi_{g,z}}{dz^2} = 4\pi G\rho_0(R) \exp\left(-\frac{\Phi_z(R, z)}{(\gamma - 1)e}\right). \quad (19)$$

Given the analytic forms of  $\Phi_{DM}$  and  $\Phi_s$  the only unknown is the potential difference of gas,  $\Phi_{g,z} = \Phi_g(R, z) - \Phi_g(R, z = 0)$ . Similar to the density method, given the boundary conditions  $\rho_0(R)$ ,  $\Phi(R, z = 0)$  and  $d\Phi(R, z = 0)/dz = 0$ , numerical integration can be applied to solve Eq. (19). By inserting  $\Phi_z$  obtained by integrating Eq. (19) into Eq. (18), the density distribution is acquired. Notice that what really matters to us is the potential difference, not the absolute value. This means the value of  $\Phi_g(R, z = 0)$  can be an arbitrary constant, although we do know the values of  $\Phi_{DM}(R, z = 0)$  and  $\Phi_s(R, z = 0)$ .

The merit of this formulation is evident, the occurrence of negative density is avoided by Eq. (18). Tiny errors in the potential difference will not do any harm to the positivity of the gas density. Numerical experiments show that in normal cases in which both the density method and potential method work, the solutions are consistent.

At a given radius,  $R$ , solving Eq. (19) only provides us with information about the potential difference,  $\Phi_z(R, z)$ . However, a useful byproduct of the potential method is that it is possible to acquire a good approximation of the total potential by:

$$\Phi_g(R, z) = \Phi_g(R, z = 0) + \Phi_{g,z}(R, z), \quad (20)$$

as long as we know the potential in the midplane,  $\Phi_g(R, z = 0)$ . Equation (20) is an approximation because the use of Eq. (19) is based on the reduced Poisson equation Eq. (14) in which the variation in radial direction is ignored. The gradient of the potential  $\Phi_g(R, z = 0)$  determines the velocity field required while the vertical potential difference  $\Phi_{g,z}(R, z)$  gives the vertical structure of the disk. In principle, the radial force, which is associated with  $\Phi_g(R, z = 0)$ ,

in the equatorial plane for an axially symmetric density distribution can be evaluated precisely by the equation (A.17) in Casertano (1983). This allows us to obtain the total potential without fully solving the Poisson equation. In practice, if the initialization is performed with multi-node clusters, each node only keeps part of the information about the density distribution, data exchange with AMR itself is technically challenging. In Section 3, for an exponential disk, the numerical results will show that the use of Eq. (29) is a good approximation for most of our interests. The corresponding  $\Phi_g(R, z = 0)$  associated with Eq. (29) can be found in the book by Binney & Tremaine (2008), Eq. (1.164a).

Equation (20) is useful, because involving the total potential into the formulation is an important step for self-consistently building up the combined disks comprised of a live stellar disk and a gas disk. Extension to the work of Shu (1969), Kuijken & Dubinski (1995, hereafter, KD95) develop a self-consistent disk-bulge-halo model for galaxies. The distribution function built by Eq. (6) in KD95 involves the potential differences  $\Phi_z$  and  $\Phi(R, 0) - \Phi(R_c, 0)$ , with  $R_c$  the radius of the guiding center. The potential method presented here can be naturally incorporated into the framework of KD95. Therefore, in this paper, all the disks are initialized by the potential method.

### 2.2.3 Exponential Disk

Some studies have assumed that the midplane density of a 3D gas disk has an exponential form (Tasker 2006, Agertz 2009). However, as we now demonstrate, in general this results in a surface density distribution that peaks at a specific non-zero radius, giving rise to a ring-like feature. We assume a gas disk with the popular  $\text{sech}^2$  vertical profile:

$$\rho_g(R, z) = \rho_c \exp(-R/R_d) \text{sech}^2\left(\frac{z}{h(R)}\right), \quad (21)$$

with  $\rho_c$  being the central volume density,  $R_d$  the disk scale-length and  $h(R)$  the scale-height as a function of radius. The surface density then reads:

$$\Sigma(R) = \int_{-\infty}^{\infty} \rho_g(R, z) dz = 2\rho_c \exp(-R/R_d) h(R). \quad (22)$$

Based on Eq. (22), we measure the scale-height of a disk at certain radius by  $h(R) = \Sigma(R)/(2\rho_0(R))$ . The extrema of the surface density can be evaluated by taking the derivative to Eq. (22):

$$\frac{d\Sigma(R)}{dR} = 2\rho_c \exp(-R/R_d) \left(\frac{dh(R)}{dR} - \frac{h(R)}{R_d}\right) = 0. \quad (23)$$

We Suppose that the disk is linearly flaring, i.e.,  $h(R) = h_0 + R/R_h$ , with  $h_0$  being the minimum scale-height of the disk and  $R_h$  a factor controlling the degree of flaring. The peak of the surface density then locates at  $R_{\text{peak}} = R_d - h_0 R_h$ . Whenever the  $R_{\text{peak}}$  is positive, we get a ring in surface density. However, a ring in the surface gas density is not commonly seen in a real disk galaxy. An exponential profile in the total gas is prevalent in disk galaxies (Leroy et al. 2008).

In order to avoid this feature, it is advantageous to specify the actual surface density of the disk, rather than its

**Table 1.** Models' Parameters.

Run	$T$ (K)	$M_s(M_\odot)$	Figure
Gas0	$4 \times 10^4$	-	(1),(2),(3)
Gas1	$2 \times 10^4$	-	(4),(5)
Gas2	$1 \times 10^4$	-	(4),(5),(8)
Gas3	$9 \times 10^3$	-	(4),(5)
Gas4	$8 \times 10^3$	-	(4),(5)
GasStar1	$7 \times 10^3$	$4 \times 10^{10}$	(6),(7),(8)
GasStar2	$6 \times 10^3$	$4 \times 10^{10}$	(6),(7)
GasStar3	$5 \times 10^3$	$4 \times 10^{10}$	(6),(7)
GasStar4	$4 \times 10^3$	$4 \times 10^{10}$	(6),(7)

\*All disks have a gas mass of  $10^{10} M_\odot$ .

midplane density. In the case of the exponential profile, the surface density reads:

$$\Sigma(R) = \Sigma_0 \exp(-R/R_d) = \int_{-\infty}^{\infty} \rho_g(R, z) dz, \quad (24)$$

with  $\Sigma_0$  being the surface density in the galactic centre. Combining Eq. (24) and Eq. (18), the volume density in the midplane can be expressed as:

$$\rho_0(R) = \frac{\Sigma_0 \exp(-R/R_d)}{\int_{-\infty}^{\infty} \exp(-\Phi_z/[(\gamma-1)e]) dz}. \quad (25)$$

It shows that the correct volume density in the midplane for the desired surface density profile can be obtained iteratively. Given a initial guess for  $\rho_0(R)$ ,  $\Phi_z$  is evaluated via Eq. (19) and also the integral appears in Eq. (25). One needs to iterate between Eq. (19) and Eq. (25). However, depending on the quality of the initial guess, convergence can be reached very fast. For instance, with the initial guess being  $\rho_0(R) = \Sigma_0 \exp(-R/R_d)$ , a six-time iteration already gives us a reasonable exponential disk.

We pursue the exponential disk for several reasons. One is simply because it is commonly seen in disk galaxies. Another is that we have a better control of the total mass. As we can see, if we specify the midplane volume density instead of the surface density, we do not exactly know the total mass until we finish the integration. Without knowing the total mass in advance, evaluating the circular velocity contributed by the self-gravity will not be a trivial task. Nevertheless, in principle, any profile of the surface density can be achieved simply by the process introduced in this sub-section.

### 3 IMPLEMENTATION AND TESTS

#### 3.1 Simulation Parameters

In this Section, we test the ideas outlined in the previous Section. We implement the method in the AMR-code RAMSES (Teyssier 2002). RAMSES uses grid-based Riemann-solvers for the magneto-hydrodynamics (MHD) and particle-mesh (PM) technique for the collisionless physics. It has a fully parallelized Poisson solver with periodic boundary conditions, which we use for this paper. Gas disks which are initialized isothermally with an exponential surface density of a scale-length of 3.5 kpc and a total mass of  $10^{10} M_\odot$  are embedded in a static potential. An isothermal equation of state is used to evolve the disks throughout this paper.

The tests are mainly divided into two groups, one group

is evolved with a static stellar potential (models with the prefix GasStar), the other without (models with the prefix Gas). Gas1 to Gas4 are M33-like gas-rich galaxies, while GasStar1 to GasStar4 are more similar to the Milky-Way. The main parameters of the models are listed in Table 1. The size of the computational domain is 250 kpc on a side. Up to 12 levels of refinement are used for those runs without stellar potential, and 13 levels for the other group, i.e., the corresponding highest spatial resolutions are about 60 pc and 30 pc, respectively.

The volume density of the halo is described by the NFW profile (Navarro, Frenk & White 1997):

$$\rho_{\text{DM}}(r) = \frac{M_{200}}{4\pi f(c)r_{200}} \frac{cx}{r^2(1+x)^2}, \quad (26)$$

with the Virial mass  $M_{200} = 10^{12} M_\odot$ ,  $x = rc/r_{200}$ , concentration parameter  $c = 12$ , distance  $r = \sqrt{R^2 + z^2}$ , Virial radius  $r_{200} = 213$  kpc and  $f(c) = \ln(1+c) - c/(1+c)$ . The Virial radius ( $r_{200}$ ) is a radius within which the averaged matter density is 200 times the critical density.

The density distribution of the stellar disk reads (Miyamoto & Nagai 1975, Binney & Tremaine 2008):

$$\rho_s(r) = \left( \frac{b^2 M_s}{4\pi} \right) \frac{aR^2 + (a + 3\sqrt{z^2 + b^2})(a + \sqrt{z^2 + b^2})^2}{[R^2 + (a + \sqrt{z^2 + b^2})^2]^{5/2} (z^2 + b^2)^{3/2}}, \quad (27)$$

with  $M_s = 4 \times 10^{10} M_\odot$  being the mass of the stellar disk,  $a = 3.5$  kpc and  $b = 0.2$  kpc the shape parameters.

In light of the result drawn from Section 2.1, for an initially constant temperature setup, we only need to know the circular velocity in the midplane for initializing the velocity field. The rotation velocity,  $V_{\text{rot}}$ , is decomposed into four components:

$$V_{\text{rot}}^2 = V_{\text{DM}}^2 + V_s^2 + V_g^2 + V_p^2, \quad (28)$$

where  $V_{\text{DM}}$ ,  $V_s$ ,  $V_g$  are the circular velocities corresponding to the dark matter halo, the stellar disk and the gas disk, and  $V_p$  denotes the contribution due to the pressure gradient.

In this paper, we have the analytic form for  $V_{\text{DM}}$  and  $V_s$ . For the contribution from the gas disk and pressure gradient, we take the approximation for an infinitesimally thin disk with exponential surface density as described in Eq. (24). We set:

$$V_g^2(R) = 4\pi G \Sigma_0 R_d y^2 [I_0(y)K_0(y) - I_1(y)K_1(y)] \quad (29)$$

$$V_p^2(R) = (\gamma - 1)e \left. \frac{\partial \ln \rho}{\partial \ln R} \right|_{z=0}, \quad (30)$$

with  $y = R/(2R_d)$ ,  $I_0$ ,  $K_0$ ,  $I_1$  and  $K_1$  being the modified Bessel functions of the first and second kinds of zeroth/first-order, respectively. Equation (30) derives from the second term of Eq. (13). However, contribution from pressure gradient in the midplane can only be evaluated after the gas disk is set up. Note that for an exponential disk, surface and volume densities decrease with radius and hence  $V_p^2$  is negative.

#### 3.2 A Stable Disk

To demonstrate that the disk built by the potential method described in Section 2 is in detailed equilibrium, we start with a stable equilibrium disk in model Gas0. In this test, the stellar disk is deliberately removed. Without the dynamical

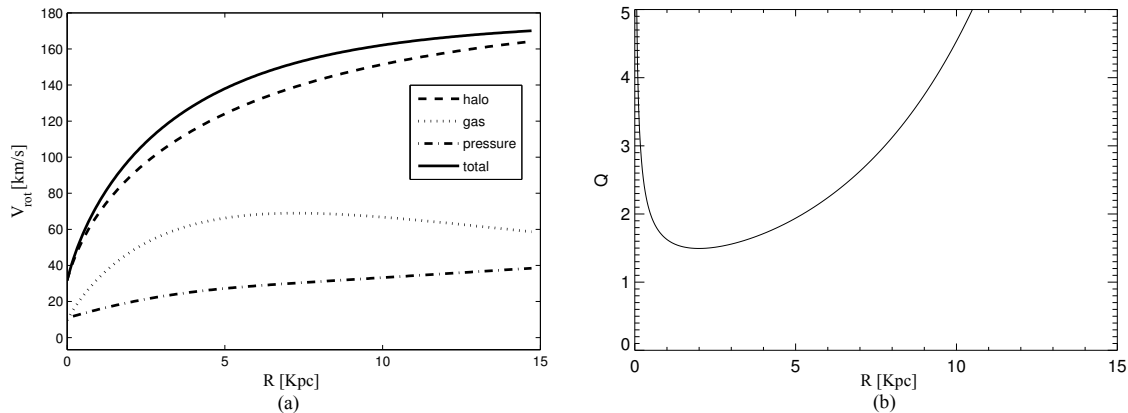


**Figure 1.** Model Gas0: (a) The total rotation velocity (solid) and contributions from dark matter halo (dashed), gas (dotted) and gas pressure (dash-dotted). Note that we plot the absolute value of the pressure gradient to have positive values for the direct comparison. It should be in opposite sense to the gravity. In this model contributions from the gas self-gravity and the pressure gradient is not negligible. (b) The  $Q$  value of model Gas0 as a function of radius as defined by Eq. (32). The  $Q$  is well above the threshold value  $Q_{\text{th}} = 1$ , thus the disk is expected to be stable. No structure should develop with time.

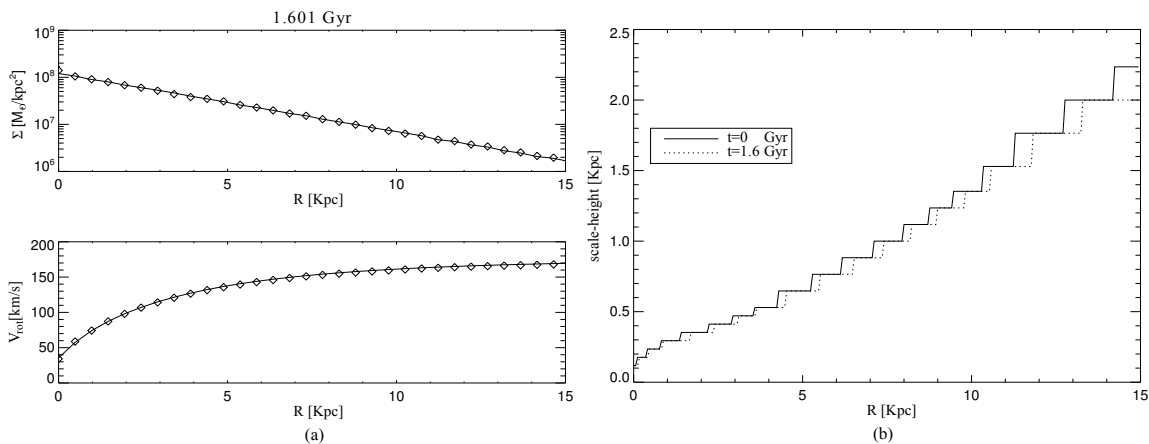


**Figure 2.** Model Gas0: The evolution of 1.6 Gyrs of a stable disk. (a) The evolution of the surface density (upper panel) and the rotation curve (lower panel) at  $t = 0$  Gyr (solid) and  $t = 1.6$  Gyr (diamond). Overall, the surface density and rotation curve are kept very well over 4 orbital periods. (b) The evolution of the scale-height at  $t = 0$  Gyr (solid) and  $t = 1.6$  Gyr (dotted). The small change in scale-height indicates that the required circular velocity is overestimated probably due to the approximation of Eq. (14) and Eq. (30). In all, the disk still stays well in the initial condition. The step-wise character of the scale-height reflects our discretization and the change of spatial resolution due to the AMR.

support from the stellar disk, the self-gravity of the gas plays the dominant role in determining the vertical structure of the disk and provides a not negligible contribution to the rotation velocity.

Figure 1a decomposes the rotation curve into the different contributions by the halo, the gas and the pressure gradient. Note that the forces of the self-gravity and the pressure gradient are in opposite sense, the self-gravity pulls inward while the pressure gradient pushes outward. In this figure,  $V_p$  is shown in its absolute value. If we ignore the pressure gradient, the disk would rotate too fast and gradually drift outward. Figure 1b shows the conventional Toomre's  $Q$  defined by:

$$Q = \frac{c_s \kappa}{\pi G \Sigma_g} \quad (31)$$

with  $\kappa$  being the epicyclic frequency. It shows that the  $Q$  is well above  $Q_{\text{th}} = 1$ , the threshold value for stability, at all

radii. The disk is hot enough to keep the disk stable and no structure should develop with time.

We let the disk evolve for 1.6 Gyrs (four orbits for the gas at 10 kpc) and check how well the disk properties are kept. Figure 2a presents the evolution of the surface density and the rotation curve. The solid lines represent the initial states and the diamond symbols are the status after an evolution of 1.6 Gyrs. The surface density is obtained by projecting along the symmetry axis and the rotation curve is evaluated by the mass-weighted circular velocity,  $\bar{v}_{\text{rot}}(R) = \int \rho_g(R, z) v_{\text{rot}}(R, z) dz / \Sigma_g(R)$ . Although a small amount of mass accretes onto the very central part of the disk, overall the surface density and the rotation curve are kept very well. Mass accretion into the center seems unavoidable for a Cartesian-grid code mainly because too small a number of cubic cells is used to mimic the circular motion

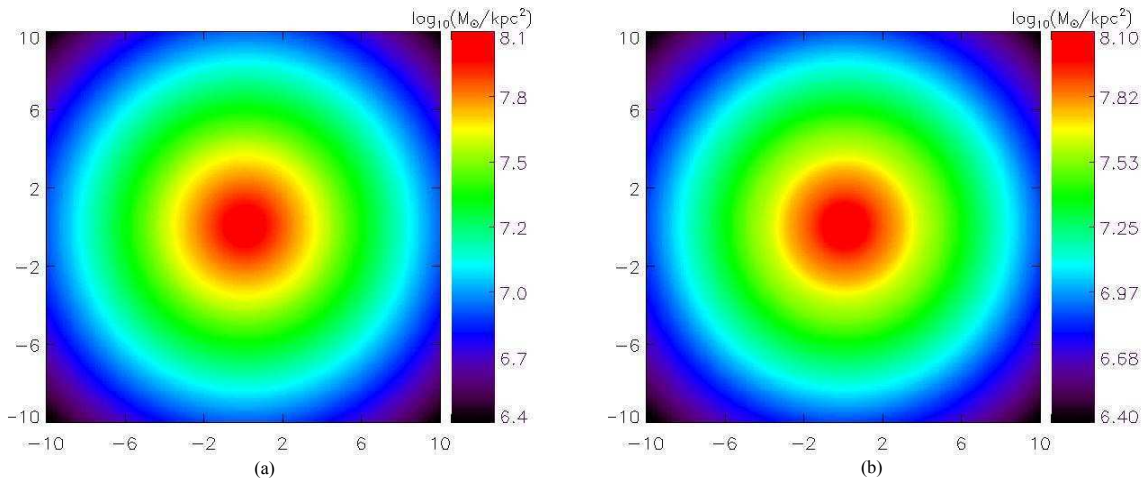


**Figure 3.** Model Gas0: The size of the images is  $20 \text{ kpc} \times 20 \text{ kpc}$ . The evolution of the surface density at (a)  $t = 0 \text{ Gyr}$  and (b) at  $t = 1.6 \text{ Gyr}$ . This figure shows that no structure is developing over secular time-scale.

in the centre. This accretion will be eventually halted by the pressure gradient built by the accumulating material.

Figure 2b shows the evolution of the scale-height. The solid line represents the initial state and the dotted line the evolution after 1.6 Gyrs. Upon closer inspection we find that the disk undergoes a very small amount of mass-redistribution in the radial direction, which we believe to be a consequence of our two approximations when initializing the disk. One is from the reduced Poisson equation, Eq. (14), and the other is from the use of Eq. (29). Equation (29) overestimates the circular velocity needed to support the disk. The thickness of the disk reduces the potential in the midplane by a few percent (see appendix B). Figure 3 shows the snapshots of the face-on surface density at  $t = 0$  (Fig. 3a) and at  $t = 1.6 \text{ Gyr}$  (Fig. 3b). No structure is developing during the course of the simulation.

To sum up, figures 1 to 3 indicate that without external perturbation the disk is quiet over secular time-scales. The shape of such a disk is naturally flaring, i.e., the scale-height increases with radius. The ideas described in Section 2 are able to treat the initial condition self-consistently. A well-balanced disk is especially useful to probe the onset of disk instability as described in the next Section.

#### 4 AXISYMMETRIC INSTABILITY

The question of disk stability has been investigated for more than four decades since the pioneering works by Toomre (1964) for collisionless stars and Goldreich & Lynden-Bell (1965) for gas sheets. Understanding the origin and evolution of disk structure is challenging. If the disk is stable like our model Gas0, no structures can form. On the other hand, if the disk is highly unstable, the surface density will quickly fragment and develop a clumpy and chaotic-looking appearance. There will be no well-organized structures. The striking spiral appearance of many nearby disk galaxies indicates that those disks are marginally stable.

For an infinitesimally thin disk, the instability threshold is at  $Q_{\text{th}} = 1$  (Toomre 1964). The first theoretical work to include the finite thickness of a self-gravitating gas disk is

that by Goldreich & Lynden-Bell (1965). Some authors have investigated the stability of finite thickness gas disks in numerical simulations (both in 2D and 3D) using local patches within a shearing box (Kim & Ostriker 2006, 2002a; Gamie 2001). This technique, in 2D, has also been used by Kim & Ostriker (2007) to investigate the interaction between the gas disk and a live stellar disk. Shetty & Ostriker (2006) used global 2D simulations in which they incorporated the effect of finite disk thickness by diluting the gravitational force. For 3D global disk calculations, see Li, Mac Low & Klessen (2005a, 2005b, 2006), who investigate the relation between disk instability and star formation rate. These studies all agree that although the inclusion of the thickness does not have a qualitative impact on the disk instability, it does shift the threshold value of instability quantitatively. In addition, accounting for disk thickness may have a large impact on the evolution of a disk, such as the development of spurs or the wiggle instability (Kim & Ostriker 2002b, 2006).

In this paper, armed with a well-balanced gas disk, we revisit the axisymmetric instability of disks in 3D global fashion. We first derive the reduction factor  $F$  which reflects the reduction of the gravity due to the finite thickness of the disk. Then the corresponding instability threshold  $Q_{\text{th}}(R, T)$  derived from a semi-analytic calculation is compared with the numerical results. In the final sub-section, we also explore the impact of the presence of a static stellar potential on the axisymmetric instability.

##### 4.1 The impact of thickness on disk stability

The Fourier component of the perturbed gravitational potential,  $\Phi_k$ , of an infinitesimally thin disk is given by:

$$\Phi_k = -\frac{2\pi G \Sigma_k}{|k|} e^{ikx - k|z|}, \quad (32)$$

where  $k$  represents the wave number of the Fourier components and  $x = R - R_0$  being the radial deviation for an axisymmetric perturbation. Supposing that a 3D disk is piled up by a stack of infinitesimally thin gas layers, we approximate the effect of the disk thickness by superimposing the contribution from every razor-thin layer:

$$\Phi_k(z) = -\frac{2\pi G \Sigma_k e^{ikx}}{|k|} \int_{-\infty}^{\infty} e^{-k|z-h|} \frac{\text{sech}^2(h/h_z)}{2h_z} dh, \quad (33)$$

with  $h_z$  being the scale-height of the disk. In Eq. (33), we model the vertical structure of the gas disk by a  $\text{sech}^2$  function. This is valid especially for the inner part of disks where the vertical structure is mainly determined by the self-gravity of the gas. See also the Fig. D1 in Appendix D. Equation (33) leads to the Fourier potential in the midplane:

$$\Phi_k(z=0) = -\frac{2\pi G \Sigma_k e^{ikx}}{|k|} F(k, h_z), \quad (34)$$

with  $F(k, h_z)$  being the reduction factor described by (see Appendix C):

$$F(k, h_z) = 1 - \frac{1}{2} k h_z \left[ H\left(\frac{k h_z}{4}\right) - H\left(\frac{k h_z}{4} - \frac{1}{2}\right) \right], \quad (35)$$

with  $H$  being the harmonic number defined by:

$$H(\alpha) = \int_0^1 \frac{1-y^\alpha}{1-y} dy. \quad (36)$$

The Lin-Shu (1964) dispersion relation for the axisymmetric perturbation is then modified to:

$$\omega^2 = \kappa^2 - 2\pi G \Sigma_0 |k| F(k, h_z) + c_s^2 k^2. \quad (37)$$

The dispersion relation states that on small scales ( $k \rightarrow \infty$ ) the disk is stabilized by gas pressure, i.e., the term  $c_s^2 k^2$ . Large scales ( $k \rightarrow 0$ ) are regulated by global shear, i.e., the  $\kappa^2$  term. The instability however happens at intermediate wavelengths, much smaller than the disk size but still larger than the thickness of the disk. In this region, neither global shear nor gas pressure can resist the gravitational collapse. The reduction factor,  $0 < F \leq 1$ , softens the effect of self-gravity and makes the disk more stable.

Given a certain radius  $R$  and temperature  $T$ , we obtain the threshold value  $Q_{\text{th}}(T, R)$  by probing the maximum value along the neutral curve defined by setting  $\omega^2 = 0$  in Eq. (37) and calculating the epicyclic frequency,  $\kappa$ , from the rotation curve. Similar to the conventional Toomre criterion for the stability of an infinitesimally thin disk,  $Q_{\text{th}}$  is a threshold curve for thick disks. Above  $Q_{\text{th}}$  the disk is stable and otherwise unstable. Since the  $Q_{\text{th}}$  is a function of both temperature and radius, it is convenient to define the critical value  $Q_{\text{crit}}$ , which is the value of  $Q_{\text{th}}$  for which  $Q_{\text{th}}(T, R)/Q(R) = 1$ , and the corresponding critical temperature  $T_{\text{crit}}$ .

The solid lines shown in Fig. 4 represent the threshold value  $Q_{\text{th}}$  as a function of radius. Each plot corresponds to a disk of different temperature. The dash-dotted lines are the actual  $Q$  values defined by Eq. (31) of the different models. From these figures, the most unstable radius is around  $R = 2$  kpc. The corresponding surface densities after an evolution of 750 Myrs are shown in Fig. 5. The gas at the most unstable region has revolved for more than four orbital periods around the disk center.

These figures shows that the prediction of  $Q_{\text{crit}}$  and the numerical results match quite well. The  $Q$  value of Gas1 is well above the solid line and shows a featureless surface density. As shown in Gas2 and Gas3, with the decrease in temperature, the  $Q_{\text{th}}$  curves shift up and the disks'  $Q$  curves come down. As a consequence, the disk starts to develop multi-armed structure, which is very likely caused by swing

amplification, as discussed in Section 5. And finally in Gas4, the curves  $Q$  and  $Q_{\text{th}}$  intersect. The disk fragments and starts to behave chaotically. A more detail calculation shows that the two curves just touch each other at a temperature  $T_{\text{crit}} = 8.5 \times 10^3 \text{K}$  with the maximum threshold  $Q_{\text{crit}} = 0.693$ , which is close to  $Q_{\text{crit}} = 0.676$  of Goldreich & Lynden-Bell's (1965) analysis but away from the numerical result,  $Q_{\text{crit}} = 0.647$ , of Kim et al. (2002a). However, the actual value of  $Q_{\text{crit}}$  is model dependent. Different models of the dark matter, the stellar disk and even the EoS will all affect the resulting value of  $Q_{\text{crit}}$ .

## 4.2 The inclusion of stellar potentials

The inclusion of a static stellar disk alters two important factors which influence the stability of the disk. One is the rotation curve and the other is the thickness of the gas disk. By changing the rotation curve, the epicyclic frequency,  $\kappa$ , changes accordingly. Supposing a flat rotation curve described by  $\Omega = V_0/R$ , the epicyclic frequency  $\kappa$  then reads:

$$\kappa^2 = 2\Omega^2 = 2\frac{V_0^2}{R^2}, \quad (38)$$

with  $V_0$  being the rotation velocity. The presence of a stellar disk tends to stabilize the gas disk via increasing  $V_0$ . However, by increasing the gravitational pull in the vertical direction, the gas disk becomes thinner and therefore more susceptible to gravitational collapse. In Section 4.1, we have already seen that the scale-height, which is governed by the temperature of the disk, is a very sensitive factor for the disk stability. GasStar1 to GasStar4 are designed to explore the competition between the two opponents.

From Fig. 6, we first notice that, compared to Fig. 4, the threshold value,  $Q_{\text{crit}}$ , is boosted from 0.693 to 0.75 due to the decrease in scale-height. This makes the disk more prone to gravitational instability. On the other hand, the change of the rotation curve drastically shifts the dash-dotted curve upwards. Instability only sets in once the temperature of the gas disk drops below  $T_{\text{crit}} \sim 6000 \text{K}$ . Overall, the presence of the static stellar disk tends to stabilize the disks.

Figure 7 shows the surface density after an evolution of 250 Myr. During this period, the gas in the most unstable region has finished 2.5 orbits. All the gas disks are developing multi-armed spiral structures within the region where the disk is the most vulnerable to instability according to Fig. 6. At this moment, the most unstable disk, GasStar4, is experiencing fragmentation. High density filaments are evident from the image. While GasStar2 is still in its early stage of instability, GasStar3 is just about to enter the fragmentation phase. GasStar1, on the other hand, does not fragments at all during the course of simulation.

The trend is clear. The cooler the disk, the faster it fragments. The spiral structure seen in these images are due to swing amplification (Toomre 1981; Goldreich & Lynden-Bell 1965), a mechanism that is capable of amplifying the perturbation by swinging the leading waves to trailing. Swing amplification is effective as the disk  $Q$  (dash-dotted line) is approaching the threshold  $Q_{\text{th}}$  (the solid line). The spirals are sheared, become tighter and tighter and enhanced. Once the density reaches the supercritical point, instability sets in.

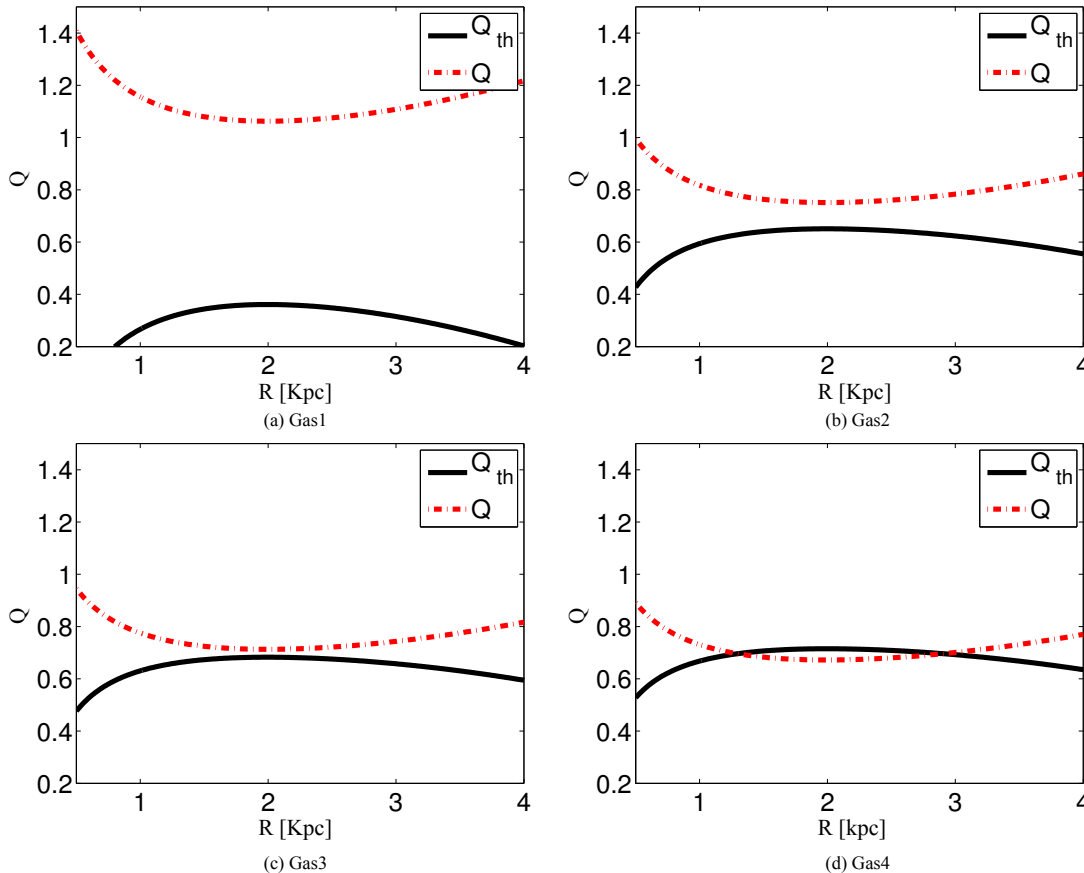


**Figure 4.** Plots (a) to (d) correspond to models from Gas1 to Gas4, respectively. In each plot, curves of the disk  $Q$  (dash-dotted) and the threshold value  $Q_{\text{th}}$  (solid) are put together to probe the onset of axisymmetric instability.  $Q_{\text{th}}(R)$  is obtained by probing the maximum value along the neutral curve for a given radius. Information of the disk thickness has been encapsulated in the reduction factor defined by Eq. (36). When the two curves meet, we expect the disk fragments very fast. This figure shows that the most unstable region is about the radius  $R = 2$  kpc. The fact that the  $Q_{\text{th}}$  curves are well below unity shows the impact of the disk thickness on the disk stability.

## 5 SPONTANEOUSLY INDUCED SPIRAL STRUCTURE

An interesting feature which is hard to ignore in Fig. 5 and Fig. 7 is that the marginally stable disks are spontaneously developing multi-arm spiral structures. We have already seen in Section 3 and 4 that the effect of the disk thickness is to shift the range of the marginally stable region downwards and therefore to stabilize the disk. As we systematically lower the temperature to probe the onset of instability, runs with as well as without stellar potential are experiencing swing amplification.

Hohl (1971) found that disks which are marginally stable to axisymmetric perturbation are prone to develop a large-scale bar structure. This finding initiated both numerical (Zang & Hohl 1978; Sellwood 1981, 1985; Fuchs & von Linden 1998; Sellwood & Moore 1999) and theoretical studies (Kalnajs 1978; Sawamura 1988; Vauterin & Dejonghe 1996; Pichon & Cannon 1997; Evans & Read 1998; Fuchs 2001) of marginally stable disks. Goldreich & Lynden-Bell (1965) and Toomre (1981) pointed out that self-gravitating, differentially rotating disks are able to amplify spiral waves by shearing a leading wave into a trailing one. Three key in-

redients, self-gravity, shearing and epicyclic motions work harmonically to make the phenomenon now coined with the name ‘swing amplification’ happen.

Three necessary conditions need to be fulfilled in order to facilitate the swing amplification (Toomre 1981; Fuchs 2001; Fuchs & von Linden 1998; Binney & Tremaine 2008). First, the disk must be marginally stable, i.e., for an infinitesimally thin disk,  $1 < Q < 2$ , as defined by Eq. (31). Second, the parameter  $X = k_{\text{crit}}R/m = k_{\text{crit}}/k_y$  (Toomre 1981; Binney & Tremaine 2008), with  $m$  being the number of arms and  $k_{\text{crit}} = \kappa^2/(2\pi G\Sigma_g)$  the critical wave number, has to be of order unity, i.e., somewhere between 1 and 3 (Goldreich & Lynden-Bell 1965; Julian & Toomre 1966; Toomre 1981). Third, there must be a mechanism that is able to induce leading arms in the system either explicitly by hand (Toomre 1981) or implicitly by random fluctuation induced by numerical noise (Toomre 1990; Sellwood & Carlberg 1984; Fuchs 2001). We notice that most of these works mentioned above are for live stellar disks not directly for the gas disk. But since the amplification principles are the same, the results are still applicable to pure gas disks.

As shown in Fig. 8a and 8b, GasStar1 gets more arms than Gas2 does. To be more quantitatively, Fig. 8c and

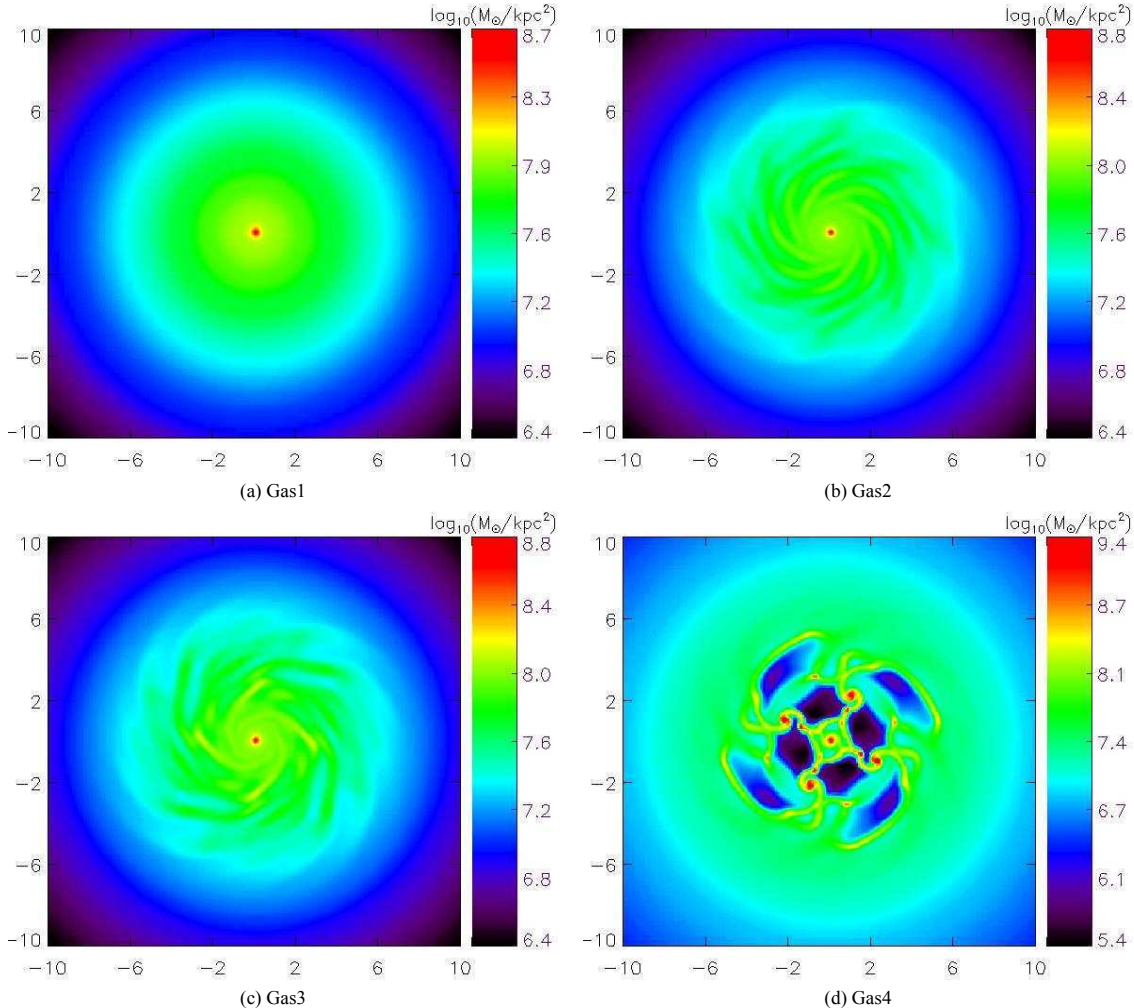


**Figure 5.** Images (a) to (d) correspond to models Gas1 to Gas4, respectively. They show the face-on surface density at  $t = 750$  Myr. The size of the images are  $20 \text{ kpc} \times 20 \text{ kpc}$ . The gas at the most unstable radius has orbited around the center for more than four times. (a) Since the disk  $Q$  is well above the threshold value  $Q_{\text{th}}$ , the disk is featureless. In models Gas2(b) and Gas3(c) the disk  $Q$  is approaching  $Q_{\text{th}}$  around  $R = 2 \text{ kpc}$ , both disks are developing self-induced spirals due to swing amplification. (d) The disk fragments very fast once  $Q$  and  $Q_{\text{th}}$  intersect.

8d show the Fourier components as a function of radius. They are obtained by doing Fourier transform to  $(\Sigma_{\text{g}}(R, \phi) - \overline{\Sigma_{\text{g}}}(R)) / \overline{\Sigma_{\text{g}}}(R)$ , where  $\overline{\Sigma_{\text{g}}}(R)$  is the averaged surface density of a given radius. Note that the dominating modes tends to be multiples of  $m = 4$ . This is a consequence of using a Cartesian grid, for which  $m = 4$  is the natural mode. However, the dominating mode is determined by physics. The dominating mode of Gas2 is  $m = 8$  while in GasStar1  $m = 12$ .

As is apparent from Eq. (38), including a stellar disk causes an increase in  $k_{\text{crit}}$ . Consequently, a larger value of  $m$  is required in order to satisfy  $1 < X < 3$ . From the image shown in Fig. 8a and the relation,  $k_{\text{crit}} \propto \kappa^2$ , to keep  $X$  a constant, the number of spiral arms in GasStar1 can be crudely estimated as  $m \simeq 15$ . More precisely, the number of spiral arms,  $m$ , is predicted by (Toomre 1981; Athanassoula, Bosma & Papaioannou 1987; Fuchs 2001, 2008):

$$m = \frac{2\pi R}{\lambda_{\text{max}}}, \quad (39)$$

with  $\lambda_{\text{max}}$  being defined by:

$$\lambda_{\text{max}} = \frac{\lambda_{\text{crit}}}{\chi(A/\Omega)}, \quad (40)$$

where  $\lambda_{\text{crit}} = 2\pi/k_{\text{crit}}$ . The coefficient  $\chi$  is a function of rotation curve (Fuchs 2001), as measured by Oort's constant  $A$ .

We employ Eq. (39) to analytically estimate the number of arms and compare the predictions with the images shown in Fig. 8. For Gas2, spirals appear between 2 kpc and 5 kpc. Within this radial range, the most unstable wavelength ranges from 2.0 to 3.6 kpc. The corresponding prediction for  $m$  ranges from 6 to 9, while the simulation reveals a spiral pattern with 8-fold symmetry. For GasStar1, spirals are prominent between 3 and 4 kpc, while the corresponding most unstable wavelength ranges from 1.4 to 2.0 kpc. The twelve arms developing in GasStar1 should be compared to a predicted  $m$  ranging from 13 to 14. Hence, overall the trends in the simulations are in reasonable agreement with our predictions. Note that the spatial resolution in both simulations

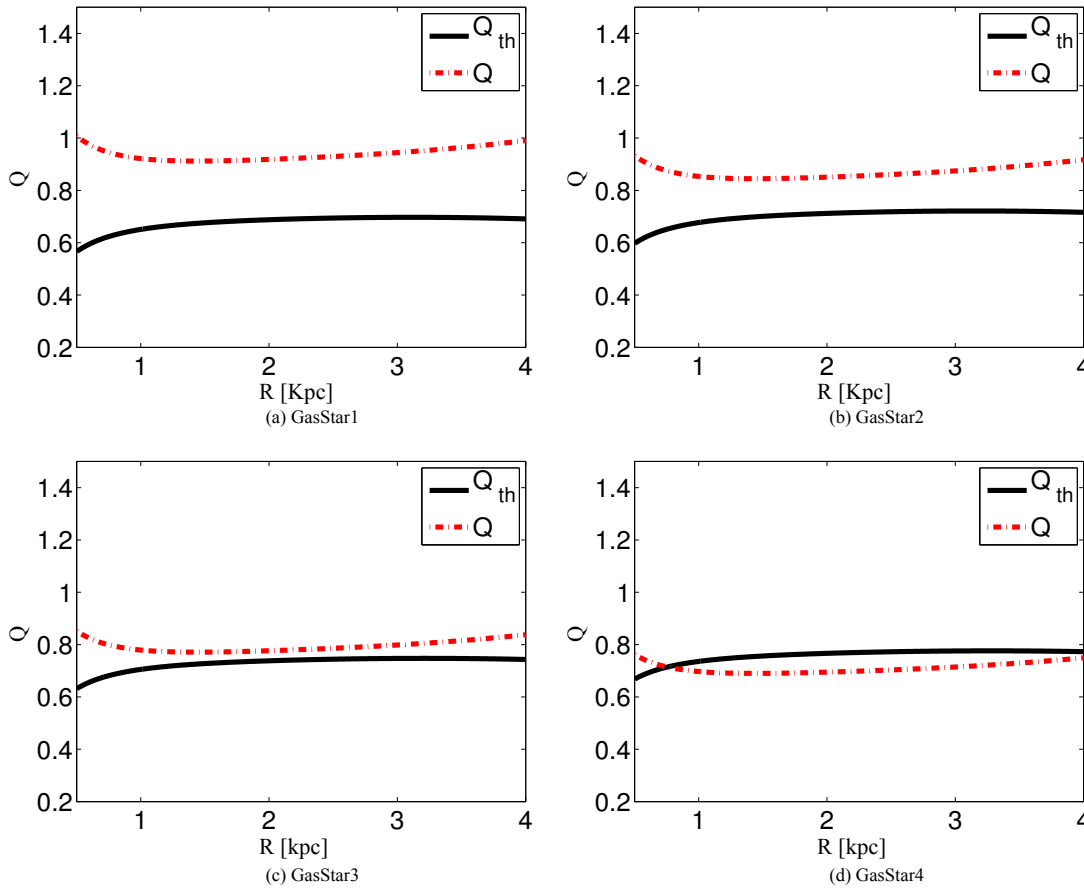


**Figure 6.** Plots (a) to (d) correspond to models GasStar1 to GasStar4, respectively: The  $Q$  (dash-dotted) and  $Q_{th}$  (solid) curves of the gas disks of different temperatures. The presence of the stellar potential stabilizes the disks through changing the rotation curve and destabilizing the disk by increasing local gravitational force. The effect of disk thickness is included via the reduction factor Eq. (36). We need to lower the temperature down to  $T = 7 \times 10^3$  K in order to probe the onset of axisymmetric instability. Overall, the presence of the stellar potential stabilizes the disk.

ranges from 60 pc to 120 pc, indicating that the most unstable wavelengths are well-resolved.

The observed small deviations can be explained as follows. First, the formulation used to predict the number of arms is precise only for stellar disks. However, Toomre (1981) has shown the strikingly similar behavior of gaseous disks (Goldreich & Lynden-Bell 1965) and stellar disks (Julian & Toomre 1966). Therefore, we have confidence that Eq. (39) is still applicable to gaseous disks. Second, the number of arms has to be an integer, a number of fraction given by Eq. (39) has no physical meaning. Third, the usage of a Cartesian grid introduces the multiples of the natural  $m = 4$  mode, which manifests itself in the Fourier transform of the surface density. Fourth, swing amplification picks up the dominating mode. It takes some time to fully develop the dominating mode. All these factors combined determine the number of spiral seen in our simulations. It is important to realize that the most unstable radius according to the axisymmetric instability criterion might not be the most effective site for swing amplification, since the shear plays an important role in this process.

Without any external pumping source, spiral waves produced by swing amplification should be a transient phe-

nomenon. Similar to material spirals, swing amplified spiral waves will experience azimuthal shearing which reduces their pitch angle until they become too tightly wound to be identified. As an example, in the Gas2 simulation, the spiral arm that appears around  $R = 2$  kpc initially has a pitch angle of  $90^\circ$  and should be sheared to less than  $1^\circ$  within 2.2 Gyr. On the contrary, we find that the spontaneously induced spirals seen in Gas2 can last for more than 3 Gyr and still keep the pitch angle relatively open. This result suggests at least one mechanism keeps replenishing noise into the disk, leaving the physics to pick up the dominating mode and sustain the waves. This noise can be caused by numerics or preexisting waves.

## 6 SUMMARY

In this paper we have developed a simple and effective method to compute the three-dimensional density and velocity structure of an isothermal gas disk in hydrodynamic equilibrium in the presence of an arbitrary external potential (i.e., dark matter halo and/or stellar disk). This is ideally suited to set-up the initial conditions of a three-dimensional gas disk in equilibrium in hydrodynamical simulations. We

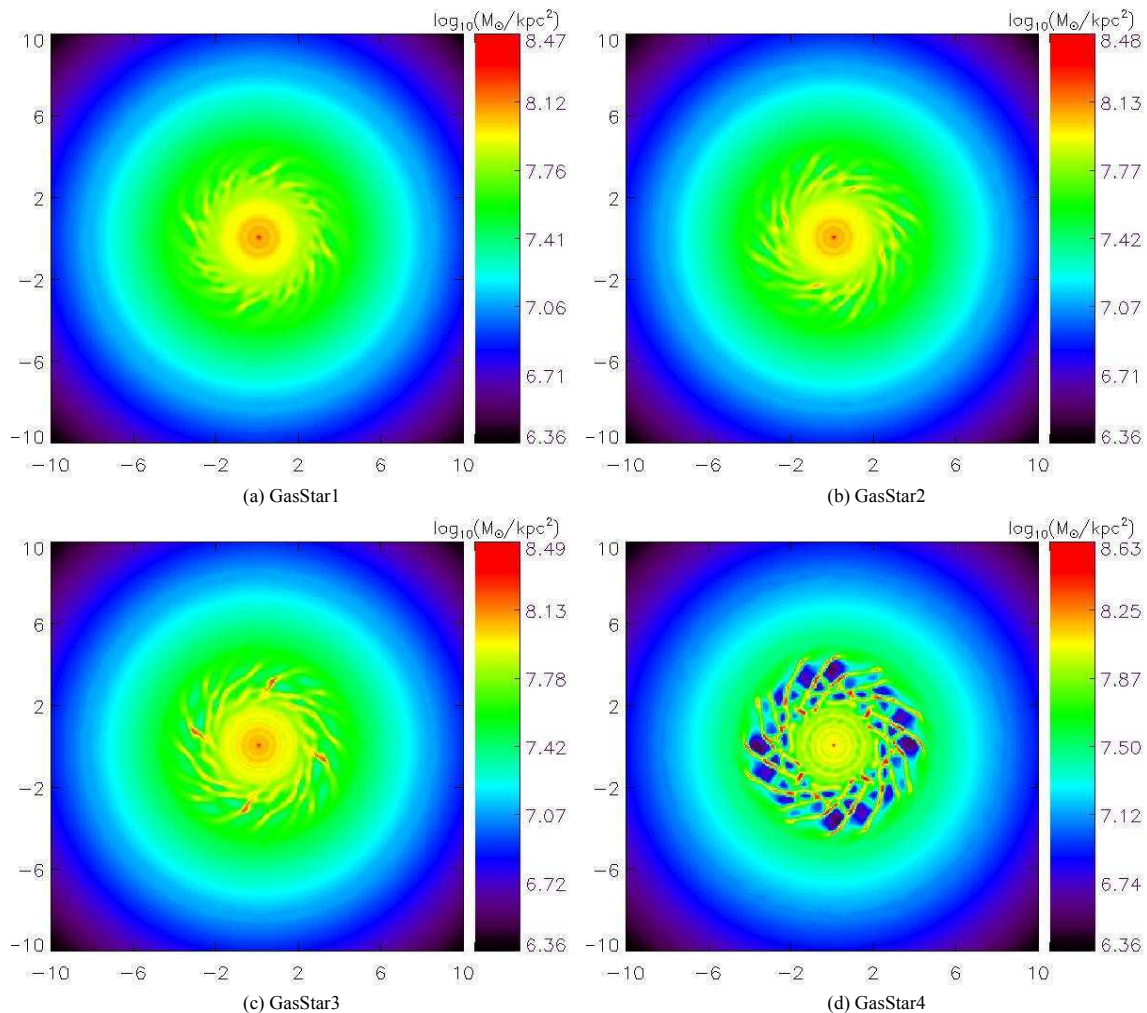


**Figure 7.** Images (a) to (d) correspond to models GasStar1 to GasStar4. They show the face-on surface density at  $t = 250$  Myr. The size of the images are  $20 \text{ kpc} \times 20 \text{ kpc}$ . The gas at the most unstable radius has orbited around the center about two and half times. Spirals seen in model GasStar2(b) and GasStar3(c) are due to swing amplification. In (d) the disk fragments very fast mainly due to both the axisymmetric instability and swing amplification.

first notice that as long as the gas is barotropic or has constant temperature at  $t = 0$ , the circular velocity needed to support the self-consistent disk is independent of the height above or below the midplane. This feature greatly simplifies the process of specifying the initial velocity field. All we need to know is the rotation velocity in the midplane.

To specify the density distribution self-consistently, the hydrostatic equation coupled with the reduced Poisson equation is adopted to develop the vertical structure of the gas. Two sets of second-order non-linear differential equations are found. One is directly associated with the gas density called the density method, the other associated with the gas potential called the potential method. In a simulation involving a huge dynamic range (using AMR techniques), the potential method is shown to be numerically more stable. A simple local iteration can be performed to gain a better control on the shape and the mass of disks. These ideas are simple enough to be incorporated into any existing code, and most importantly they are very effective.

With gas disks that are in detailed balance, we are able to systematically investigate the axisymmetric stability of a

fully three-dimensional disk for the first time. We probe the onset of instability both semi-analytically and numerically. Simulations without stellar disk show that the thickness of the gas disk, which is governed by the temperature of the disk, has a huge impact on the disk stability. The reduction of the gravity decreases the threshold value by around 30 percent in our models. As we gradually lower the gas temperature, the threshold  $Q_{\text{th}}$  shifts up, the disk  $Q$  shifts down, and the system starts to develop multi-arm structure via swing amplification. The onset of the instability in simulations matches the theoretical prediction very well as shown in Fig. 4 and Fig. 5. The disk fragments as the two curves,  $Q$  and  $Q_{\text{th}}$ , come very close to each other.

The influence of the stellar disk is less obvious. Its presence has a stabilizing effect on the gas disk through changing the rotation curve and a destabilizing one through the increase of the local gravitational force. The simulation results show that overall the presence of the stellar disk tends to stabilize the gas disk. But this conclusion comes with a caveat. The interaction between live stars and gas might be important. A live stellar disk itself can be unstable or marginally

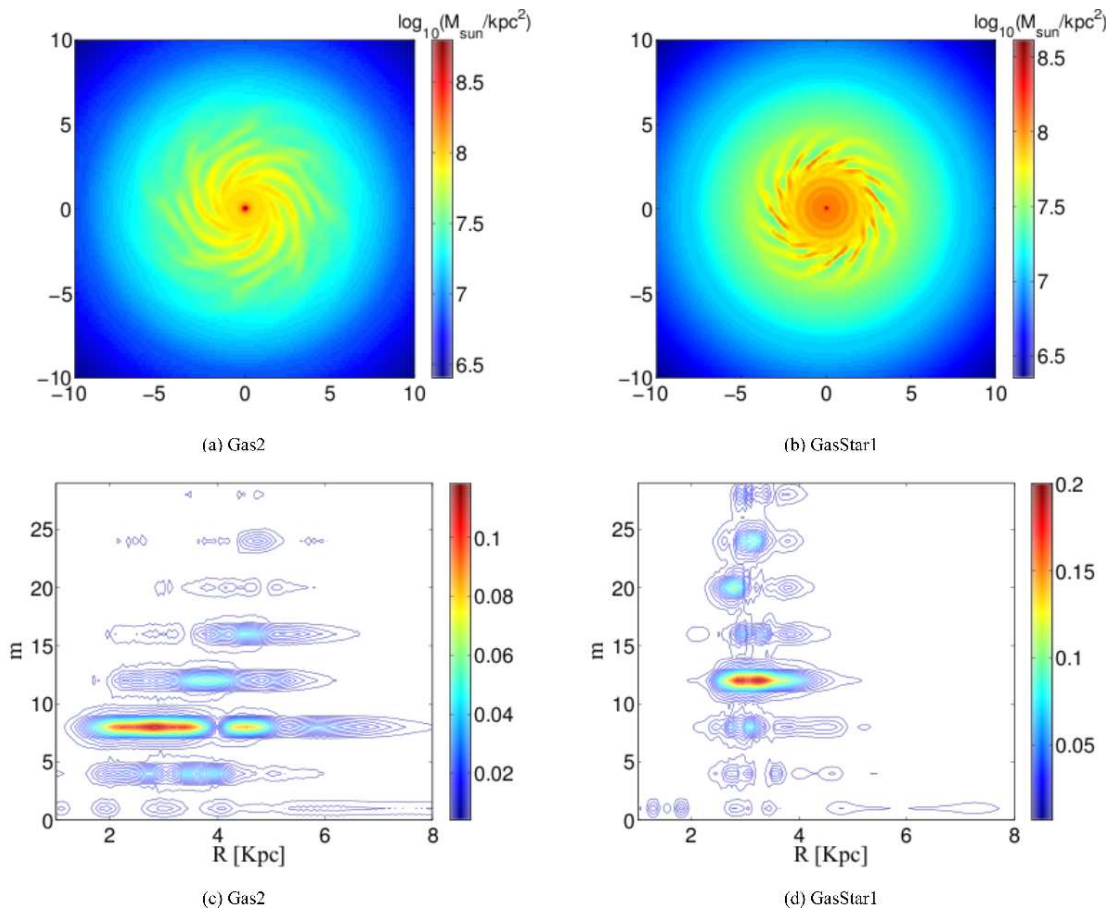


**Figure 8.** The image size in (a) and (b) is  $20 \text{ kpc} \times 20 \text{ kpc}$ . (a) The surface density of Gas2 at  $t = 750 \text{ Myr}$ . (b) The surface density of GasStar1 at  $t = 500 \text{ Myr}$ . In both cases, the inner parts of the gas disks, which have been evolved for about four orbital times, developing spiral structure. Contour plots (c) and (d) are the Fourier maps of (a) and (b), respectively. In (c) and (d), the horizontal axis represents radius, the vertical axis is the number of arms,  $m$ , obtained by Fourier analysis. The color represents the intensity of each Fourier mode, the redder the stronger.

stable. Perturbations from the interstellar medium can trigger instabilities in the stellar disk. Since stars dominate the mass budget in Milky-Way type galaxies (more than 90 percent), and because gas is highly responsive and dissipative, the interplay between both components is one of the most interesting subjects in galactic dynamics. Tackling this problem needs elaborate initial conditions for the live stellar disk or the combined disk. We stress that the potential method developed in this paper is compatible with the formulation in KD95. This makes the self-consistent combined disk a natural direction for future work.

Marginally stable disks are susceptible to the process of swing amplification, a prevalent mechanism that triggers self-induced spirals. Simulations Gas2 and GasStar1 show the spirals are prominent in the regions in which the gas can respond to swing amplification. Semi-analytic result relates the most vulnerable wavelength in azimuthal direction,  $\lambda_{\text{max}}$ , to the number of arms. Numerically, The natural mode of a Cartesian grid together with the swing amplification determine the dominating mode of the spiral structure. Our numerical results with or without stellar disk shows the correct characteristics of the swing amplification. It happens in marginally stable disks and the number of arm fits reasonably well to the analytic prediction. In the run of GasStar2,

swing amplification eventually leads to disk fragmentation once the density becomes supercritical to the gravitational instability. However, in a sub-critical case like Gas2, the spiral structure can survive more than 3 Gyrs without fragmenting the disk, suggesting at least one mechanism is sustaining the waves. The number of arms suggests a characteristic wavelength relating to the upper limit of the mass of giant molecular clouds (Escala 2008).

## ACKNOWLEDGMENTS

R.S.K. acknowledges financial support from the German *Bundesministerium für Bildung und Forschung* via the ASTRONET project STAR FORMAT (grant 05A09VHA) and from the *Deutsche Forschungsgemeinschaft* (DFG) under grants no. KL 1358/1, KL 1358/4, KL 1359/5, KL 1359/10, and KL 1359/11. R.S.K. furthermore thanks for subsidies from a Frontier grant of Heidelberg University sponsored by the German Excellence Initiative and for support from the *Landesstiftung Baden-Württemberg* via their program International Collaboration II (grant P-LS-SPII/18). R.S.K. also thanks the KIPAC at Stanford University and the Department of Astronomy and Astrophysics at the University of

California at Santa Cruz for their warm hospitality during a sabbatical stay in spring 2010. H.-H.W. acknowledges the financial support from the International Max Planck Research School (IMPRS) Heidelberg and the technical support with RAMSES from Dr. R. Teyssier. Authors acknowledge the anonymous referee's comments and discussions that make this paper better. Numerical simulations were performed on the PIA cluster of the Max-Planck-Institut für Astronomie at the Rechenzentrum in Garching.

## REFERENCES

- Agertz O., Lake G., Teyssier R., Moore B., Mayer L., Romeo A.B., 2009, MNRAS, 392, 294
- Athanassoula E., Bosma A., Papaioannou S. 1987, A&A, 179, 23
- Binney J., Tremaine S. 2008, Galactic Dynamics (Princeton: Princeton Univ. Press, 2nd Ed.)
- Casertano S., 1983, MNRAS, 203, 735
- Escala A., Larson R.B., 2008, ApJ, 685, L31
- Evans N.W., Read J.C.A., 1998, MNRAS, 300, 106
- Fuchs B., 2001, A&A, 368, 107
- Fuchs B., 2008, Invited contribution to Galactic and Stellar Dynamics in the era of high resolution surveys, Strassburg, March 16-20 [arXiv:0810.3503]
- Fuchs B., von Linden S., 1998, MNRAS, 294, 513
- Gammie C.F., 2001, ApJ, 553, 174
- Goldreich P., Lynden-Bell D., 1965, MNRAS, 130, 125
- Gradshteyn I. S., Ryzhik I. M., 1965, Table of Integrals, Series, and Products, 4th Ed. (Academic Press, New York)
- Hohl F. 1971, ApJ, 168, 343
- Jackson, P.D., Kellman, S.A., 1974, ApJ, 190, 53
- Julian W.H., Toomre A., 1966, ApJ, 146, 810 (JT)
- Kalnajs A.J., 1978, In IAU Symposium 77, Structure and Properties of Nearby Galaxies, ed. Berkhuijsen E.M., Wielebinski R. (Dordrecht: Reidel), 133
- Kent, S. M., Dame, T. M., Fazio, G. 1991, ApJ, 378, 131
- Kim W.T., Ostriker E.C., 2007, ApJ, 660, 1232
- Kim W.T., Ostriker E.C., 2006, ApJ, 646, 213
- Kim W.T., Ostriker E.C., Stone J.M., 2002a, ApJ, 581, 1080
- Kim W.T., Ostriker E.C., 2002b, ApJ, 570, 132
- Kuijken K., Dubinski J., 1995, MNRAS, 277, 1341
- Leroy A.K., Walter F., Brink E., Bigiel F., de Blok W.J.G., Modore B., Thornley M.D. 2008, AJ, 136, 2782
- Li X., Mac Low M.-M., Klessen R.S., 2005a, ApJ, 620, 19
- Li X., Mac Low M.-M., Klessen R.S., 2005b, ApJ, 626, 823
- Li X., Mac Low M.-M., Klessen R.S., 2006, ApJ, 639, 879
- Lin C.C., Shu F.H., 1964, ApJ, 140, 646
- Lisker T., Fuchs B., 2009, A&A, 501, 429
- Lockman, F. J. 1984, ApJ, 283, 90
- Miyamoto M., Nagai R., 1975, Astron. Soc. Japan, 27, 533
- Narayan C.A., Jog C.J., 2002, A&A., 394, 89
- Navarro J., Frenk C., White S.D.M., 1997, ApJ, 490, 493
- Pichon C., Cannon R.C., 1997, MNRAS, 291, 616
- Rafikov R. R., 2001, MNRAS, 323, 445
- Sanders, D. B., Solomon, P. M., Scoville, N. Z. 1984, ApJ, 276, 182
- Sawamura M., 1988, PASJ, 40, 279
- Sellwood J.A., Moore E.M., 1999, ApJ, 510, 125
- Sellwood J.A., 1985, MNRAS, 217, 127
- Sellwood J.A., Carlberg R.G., 1984, ApJ, 282, 61
- Sellwood J.A., 1981, A&A, 99, 362
- Shetty R., Ostriker E.C., 2006, ApJ, 647, 997
- Shu F.H., 1969, 158, 505
- Spitzer L., JR., 1942, ApJ, 95, 329
- Springel V., Matteo T.D., Hernquist L., 2005, MNRAS, 361, 776
- Tasker E., Bryan G., 2006, ApJ, 641, 878
- Teyssier R., 2002, A&A, 385, 337
- Toomre A., 1990, in Dynamics and Interactions of Galaxies, ed. R. Wielen (Springer, Berlin), 292
- Toomre A., 1981, in Structure and Evolution of Normal Galaxies, ed. Fall, S.M., Lynden-Bell, D. (Cambridge: CUP), 111
- Toomre A., 1964, ApJ, 139, 1217
- van der Kruit, P. C., Searle, L. 1981a, A&A, 95, 105
- van der Kruit, P. C., Searle, L. 1981b, A&A, 95, 116
- Vauterin P., Dejonghe H., 1996, A&A, 313, 465
- Wouterloot, J. G. A., Brand, J., Burton, W. B., Kwee, K. K. 1990, A&A, 230, 21
- Zang T.A., Hohl F. 1978, ApJ, 226, 521

## APPENDIX A: THE DERIVATION OF ROTATION VELOCITY

Equation (11) can be re-written as

$$p(R, z) = \rho(R, z) \frac{p(R)}{\rho(R)} \Big|_{z=0} - \rho(R, z) \int_0^z \frac{p}{\rho^2} \frac{\partial \rho}{\partial z} dz - \rho(R, z) [\Phi(R, z) - \Phi(R, z=0)], \quad (\text{A1})$$

where we have replaced  $\Phi_z = \Phi(R, z) - \Phi(R, z=0)$ . Inserting Eq. (A1) in Eq. (1) involves a partial derivative to the integral, let us prepare it first:

$$\begin{aligned} \frac{\partial}{\partial R} \left( \int_0^z \frac{p}{\rho^2} \frac{\partial \rho}{\partial z} dz \right) &= \int_0^z \frac{\partial}{\partial R} \left( \frac{p}{\rho^2} \frac{\partial \rho}{\partial z} \right) dz \\ &= \int_0^z \left\{ \frac{\partial^2}{\partial R \partial z} \left( \frac{p}{\rho^2} \right) - \frac{\partial}{\partial R} \left[ \rho \frac{\partial}{\partial z} \left( \frac{p}{\rho^2} \right) \right] \right\} dz \\ &= \int_0^z \left\{ \frac{\partial}{\partial z} \left[ \frac{p}{\rho^2} \frac{\partial \rho}{\partial R} + \rho \frac{\partial}{\partial R} \left( \frac{p}{\rho^2} \right) \right] - \frac{\partial}{\partial R} \left[ \rho \frac{\partial}{\partial z} \left( \frac{p}{\rho^2} \right) \right] \right\} dz \\ &= \frac{p(R, z)}{\rho(R, z)} \frac{\partial \ln \rho(R, z)}{\partial R} - \frac{p(R, z=0)}{\rho(R, z=0)} \frac{\partial \ln \rho(R, z=0)}{\partial R} \\ &\quad + \int_0^z \left\{ \left( \frac{\partial \rho}{\partial z} \right) \frac{\partial}{\partial R} \left( \frac{p}{\rho^2} \right) - \left( \frac{\partial \rho}{\partial R} \right) \frac{\partial}{\partial z} \left( \frac{p}{\rho^2} \right) \right\} dz \quad (\text{A2}) \end{aligned}$$

With Eq. (A2), the first term of Eq. (1) then becomes:

$$\begin{aligned} \frac{1}{\rho(R, z)} \frac{\partial p(R, z)}{\partial R} &= \frac{\partial}{\partial R} \left( \frac{p(R, z=0)}{\rho(R, z=0)} \right) \\ &\quad - \left[ \frac{\partial \Phi(R, z)}{\partial R} - \frac{\partial \Phi(R, z=0)}{\partial R} \right] \\ &\quad + \frac{p(R, z=0)}{\rho(R, z=0)} \frac{\partial \ln \rho(R, z=0)}{\partial R} \\ &\quad - \int_0^z \left\{ \left( \frac{\partial \rho}{\partial z} \right) \frac{\partial}{\partial R} \left( \frac{p}{\rho^2} \right) - \left( \frac{\partial \rho}{\partial R} \right) \frac{\partial}{\partial z} \left( \frac{p}{\rho^2} \right) \right\} dz \\ &\quad + \frac{\partial \ln \rho(R, z)}{\partial R} \left\{ \frac{p(R, z=0)}{\rho(R, z=0)} - \frac{p(R, z)}{\rho(R, z)} \right\} \\ &\quad - \left\{ \Phi(R, z) + \Phi(R, z=0) - \int_0^z \frac{p}{\rho^2} \frac{\partial \rho}{\partial z} dz \right\} \quad (\text{A3}) \end{aligned}$$

Equation (11) says that the term in the big brace should vanish. And therefore, Eq. (1) reduces to

$$\begin{aligned} \frac{1}{\rho} \frac{\partial p}{\partial R} + \frac{\partial \Phi}{\partial R} &= \frac{\partial}{\partial R} \left[ \frac{p(R, z=0)}{\rho(R, z=0)} \right] \\ &\quad + \frac{\partial \Phi(R, z=0)}{\partial R} + \frac{p(R, z=0)}{\rho(R, z=0)} \frac{\partial \ln \rho(R, z=0)}{\partial R} \end{aligned}$$

$$- \int_0^z \left\{ \left( \frac{\partial \rho}{\partial z} \right) \frac{\partial}{\partial R} \left( \frac{p}{\rho^2} \right) - \left( \frac{\partial \rho}{\partial R} \right) \frac{\partial}{\partial z} \left( \frac{p}{\rho^2} \right) \right\} dz \quad (\text{A4})$$

For the barotropic gas, i.e.,  $p(\rho)$ , the integrand of the integral vanishes:

$$\begin{aligned} & \left( \frac{\partial \rho}{\partial z} \right) \frac{\partial}{\partial R} \left( \frac{p}{\rho^2} \right) - \left( \frac{\partial \rho}{\partial R} \right) \frac{\partial}{\partial z} \left( \frac{p}{\rho^2} \right) \\ &= \left( \frac{\partial \rho}{\partial z} \right) \frac{\partial}{\partial \rho} \left( \frac{p}{\rho^2} \right) \frac{\partial \rho}{\partial R} - \left( \frac{\partial \rho}{\partial R} \right) \frac{\partial}{\partial \rho} \left( \frac{p}{\rho^2} \right) \frac{\partial \rho}{\partial z} = 0 \end{aligned} \quad (\text{A5})$$

For the cases of initially constant temperature, the specific internal energy,  $e$ , is a constant and therefore the pressure is a function of density only, the integrand vanishes.

## APPENDIX B: THE EFFECT OF THE DISK THICKNESS ON THE MIDPLANE POTENTIAL

For an axisymmetrically and infinitesimally thin disk, the potential can be evaluated by the following relation (Binney & Tremaine, 2008):

$$\Phi(R, z) = \int_0^\infty dk S_0(k) J_0(kR) e^{-k|z|}, \quad (\text{B1})$$

where  $J_0$  is the Bessel function of the first kind of order zero and  $S_0$  is the Hankel transform of  $-2\pi G \Sigma_0$  defined by:

$$S_0(k) = -2\pi G \int_0^\infty dR' R' J_0(kR') \Sigma_0(R') \quad (\text{B2})$$

With Eq. (B1) and Eq. (B2), we can superimpose the potential contributed by each gas layer. For the sake of simplicity, we assume that the volume density has the double exponential profile:

$$\rho_0(R, z) = \Sigma_0 e^{-R/R_d} \frac{e^{-z/h_z}}{2h_z}, \quad (\text{B3})$$

with  $h_z$  being the scale-height of the gaseous disk, Eq. (B2) then becomes (Gradshteyn & Ryzhik 1965, hereafter GR65, 6.623-2):

$$\begin{aligned} S_0(k, z) &= \frac{-2\pi G \Sigma_0 e^{-z/h_z}}{2h_z} \Delta z \int_0^\infty dR' R' J_0(kR') e^{-R'/R_d} \\ &= \frac{-2\pi G \Sigma_0 e^{-z/h_z}}{2h_z} \Delta z \frac{\xi}{(\xi^2 + k^2)^{3/2}}, \end{aligned} \quad (\text{B4})$$

with  $\xi = 1/R_d$ .  $\Delta z$  represents the infinitesimal thickness introduced to keep the dimension correct. The potential which takes into account the thickness of the disk then reads:

$$\begin{aligned} \Phi(R, z) &= -2\pi G \Sigma_0 \int_0^\infty dk \frac{\xi}{(\xi^2 + k^2)^{3/2}} J_0(kR) \\ &\quad \times \int_{-\infty}^\infty e^{-k|z-h|} \frac{e^{-h/h_z}}{2h_z} dh. \end{aligned} \quad (\text{B5})$$

Evaluating the potential at the midplane,  $z = 0$ , yields:

$$\Phi(R, z = 0) = -2\pi G \Sigma_0 \int_0^\infty dk \frac{\xi}{(\xi^2 + k^2)^{3/2}} J_0(kR) \frac{1}{1 + kh_z}. \quad (\text{B6})$$

Given the finite scale-height, the integral can be evaluated numerically and compared with the result of the infinitesimally thin disk.

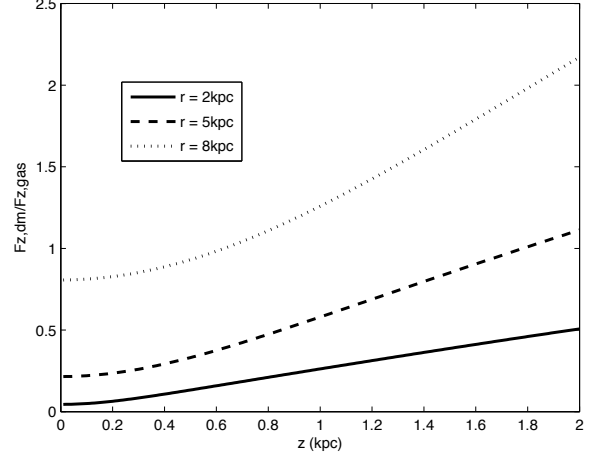


**Figure D1.** The force ratio  $F_{z,DM}/F_{z,gas}$  at  $R=2, 5$  and  $8$  kpc. It shows that the vertical structure of the inner disk is determined mostly by the self-gravity of gas.

## APPENDIX C: THE DERIVATION OF THE REDUCTION FACTOR

To derive the reduction factor  $F$  defined by Eq. (35) we need to evaluate the integral of the form:

$$\begin{aligned} \int_{-\infty}^\infty e^{-k|h|} \text{sech}^2(ah) dh &= 2 \int_0^\infty e^{-kh} \text{sech}^2(ah) dh \\ &= \frac{2}{a} \left\{ 1 - \frac{k}{2a} \left[ H\left(\frac{k}{4a}\right) - H\left(\frac{k}{4a} - \frac{1}{2}\right) \right] \right\}. \end{aligned} \quad (\text{C1})$$

The last line can be reached by looking up the formulae 3.541, 8.370, 8.361-7 listed in the integral table (GR65) and the definition Eq. (36). In the last line, we have employed the recursive relation (8.365-1 GR65):

$$H(\alpha) = H(\alpha - 1) + \frac{1}{\alpha}. \quad (\text{C2})$$

The asymptotic behavior of the harmonic number reads (8.367-2, 8.367-13 GR65):

$$H(\alpha) = \ln \alpha + \gamma + \frac{1}{2}\alpha^{-1} - \frac{1}{12}\alpha^{-2} + \frac{1}{120}\alpha^{-4} + O(\alpha^{-6}), \quad (\text{C3})$$

with  $\gamma = 0.5772156649$  (8.367-1 GR65) being the Euler-Mascheroni constant. Note that Eq. (C3) is only reliable when  $\alpha \geq 1$ . We employ the recursive relation (C2) to evaluate  $H(\alpha)$  for  $-1 < \alpha < 1$ .

## APPENDIX D: THE VERTICAL FORCE RATIO

The vertical force ratio measures the impact of the halo force on the vertical structure. The simplified Poisson equation for isothermally self-gravitating gas disk reads:

$$\frac{\partial^2 \Phi_g}{\partial z^2} = 4\pi G \rho_0(R) \text{sech}^2\left(\frac{z}{h_z}\right), \quad (\text{D1})$$

where  $h_z$  being a measure of the scale-height. Parameter  $h_z$  can be related to the volume density in the midplane,  $\rho_0(R)$  by:

$$h_z = \sqrt{\frac{c_s^2}{2\pi G \rho_0}}. \quad (\text{D2})$$

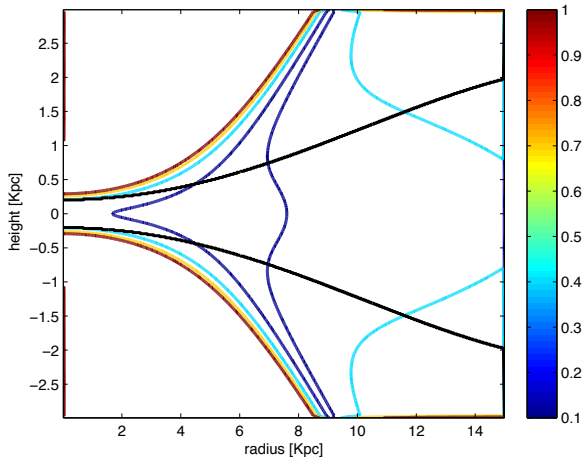


**Figure E1.** Contour map of  $\epsilon$ . The black lines represent the scale-height of the gas disk.

The corresponding vertical force for the gas then becomes:

$$F_{z,\text{gas}} = -\frac{\partial\Phi}{\partial z} = -4\pi Gh_z\rho_0(R)\tanh(z/h_z). \quad (\text{D3})$$

For a NFW halo, the vertical force can be written down directly:

$$F_{z,\text{DM}} = \frac{GM_{200}}{f(c)} \left(\frac{c}{r_{200}}\right)^2 \frac{x/(1+x) - \ln(1+x)}{x^2} \frac{z}{\sqrt{R^2 + z^2}}, \quad (\text{D4})$$

with  $x = c\sqrt{R^2 + z^2}/r_{200}$ . Figure D1 then shows the force ratio  $F_{z,\text{DM}}/F_{z,\text{gas}}$  as a function of vertical height  $|z|$  at different radii. Comparing to the rotation curve shown in the left panel of Fig. 1, although the dynamics is still dictated by the potential of the dark halo, the vertical structure of the gaseous disk is mainly determined by the self-gravity of the gas component. However, it raises another issue, the presence of the stellar disk will dominate both the dynamics and the vertical structure of the gas and will affect the stability of the gas component via changing the thickness of the gaseous disk and the rotation curve.

## APPENDIX E: VALIDITY CHECK OF THE REDUCED POISSON EQUATION FOR THE GAS DISK

Throughout this paper we have assumed that the radial potential gradients of the disk are negligible compared to the vertical gradients, such that the Poisson equation reduces to Eq. (14). We now test this assumption by computing the ratio

$$\epsilon \equiv \left| \frac{1}{R} \frac{\partial}{\partial R} \left( R \frac{\partial\Phi_g}{\partial R} \right) / \frac{\partial^2\Phi_g}{\partial z^2} \right|, \quad (\text{E1})$$

with  $\Phi_g$  the gravitational potential of the gas disk. For a realistic, analytical disk model, our assumption will be valid as long as  $\epsilon \ll 1$ .

Consider the Miyamoto & Nagai (1975) potential:

$$\Phi_g(R, z) = -\frac{GM_g}{\sqrt{R^2 + (a + \sqrt{z^2 + b^2(R)})^2}}. \quad (\text{E2})$$

Here  $a$  is a constant that controls the scale-length of the disk and  $b(R)$ , which we take to be a function of radius, modulates the scale-height of the disk. In the limit  $b \rightarrow 0$  this model reduces to the infinitesimal Kuzmin disk (e.g., Binney & Tremaine 2008). In an attempt to model the gas disk in our simulation ‘Gas0’, we adopt  $a = 3.5$  kpc. In order to mimic the flaring of the Gas0 disk (see Fig. 2b), we consider

$$b(R) = -1.58 \times 10^{-5} R^4 + 1.21 \times 10^{-2} R^2 + 0.20. \quad (\text{E3})$$

Using the Poisson equation to solve (numerically) for the corresponding density distribution yields the radial-dependent scale-height shown as the solid black lines in Fig. E1, and which is comparable to that of the Gas0 disk. The contours in Fig. E1 are defined by constant values of  $\epsilon$ . These show that our assumption that  $\epsilon \ll 1$  is well-justified in the inner part of the disk, out to  $\sim 3$  scale-lengths, which encloses most of the disk mass. The assumption that  $\epsilon \ll 1$  deteriorates at larger radii and at higher altitude away from the midplane. This might be in part responsible for the very slight outward drifting of the disk seen in Fig. 2b. In cases that include a stellar potential and/or cooler gas, the gas disk is even thinner than the case considered here, resulting in values for  $\epsilon$  that are even smaller. Based on these results, and based on the absence of significant disk thickening in our simulations, we are confident that Eq. (14) is sufficiently accurate for all realistic gas disks.